https://doi.org/10.5194/amt-2020-336
Preprint. Discussion started: 17 September 2020

Atmospheric Measurement Techniques Discussions

Integration of GOCI and AHI Yonsei Aerosol Optical Depth Products During the 2016 KORUS-AQ and 2018 EMeRGe Campaigns

Hyunkwang Lim[1], Sujung Go[1,2], Jhoon Kim[1], Myungje Choi[2,3], Seoyoung Lee[1], Chang-Keun Song[4], Yasuko Kasai[5]

[1]Department of Atmospheric Sciences, Yonsei University, Seoul 03722, Republic of Korea
[2]Joint Center for Earth Systems Technology, University of Maryland Baltimore County, Baltimore, MD, USA
[3]Jet Propulsion Laboratory, California Institute of Technology, Pasadena, CA, USA
[4]School of Urban and Environmental Engineering, Ulsan National Institute of Science and Technology, Ulsan 44919, Republic of Korea
[5]Natinal Institute of Information and Communications Technology, Tokyo 184-8759, Japan

Correspondence to: Jhoon Kim (jkim2@yonsei.ac.kr)

Abstract. The Yonsei AErosol Retrieval (YAER) algorithm for the Geostationary Ocean Color Imager (GOCI) retrieves aerosol optical properties only over dark surfaces, so it is important to mask pixels with bright surfaces. The Advanced Himawari Imager (AHI) is equipped with three shortwave-infrared and nine infrared channels, which is advantageous for bright-pixel masking. In addition, multiple visible and near-infrared channels provide a great advantage in aerosol property retrieval from the AHI and GOCI. By applying the YAER algorithm to 10 minutes AHI or 1 hour GOCI data at 6 km × 6 km resolution, diurnal variations and aerosol transport can be observed, which has not previously been possible from low-earth-orbit satellites. This study attempted to estimate the optimal aerosol optical depth (AOD) for East Asia by data fusion, taking into account satellite retrieval uncertainty. The data fusion involved two steps: (1) analysis of error characteristics of each retrieved result with respect to the ground-based Aerosol Robotic Network (AERONET), and bias correction based on normalized difference vegetation indexes; and (2) estimation of the fused product using ensemble-mean and maximum-likelihood estimation methods. Fused results show a better statistics in terms of fraction within the expected error, correlation coefficient, root-mean-square error, median bias error than the retrieved result for each product.

1. Introduction

Aerosols are generated by human activities and natural processes on local to global scales, and have a lifetime of several to tens of days. Aerosols affect radiative energy by scattering and absorption (e.g. Cho et al., 2003). High aerosol loadings are persistent in Northeast Asia, including diverse aerosol types from various sources. Interactions among aerosols, clouds, and radiation in the atmosphere cause significant uncertainties in climate-model calculations (IPCC, 2013). Datasets produced by satellites have been widely used to reduce such uncertainties (Saide et al., 2014; Pang et al., 2018), but the

https://doi.org/10.5194/amt-2020-336
Preprint. Discussion started: 17 September 2020


Atmospheric Measurement Techniques Discussions

systems must be accurately calibrated, verified, and consistent. Satellite data have been used extensively to retrieve aerosol optical properties (AOPs) over broad areas, with several algorithms having been developed (Knapp et al., 2005; Remer et al., 2005; Kim et al., 2008; Lyapustin et al., 2011a, b; Lee et al., 2012; Fukuda et al., 2013; Hsu et al., 2013; Levy et al., 2013; Kim et al., 2014, 2016; Choi et al., 2016, 2018; Garay et al., 2017, 2020; Kikuchi et al., 2018; Li, et al., 2018). Sun-synchronous orbit (SSO) satellites pass over the same area each day at approximately the same local time. Satellites in low earth orbit (LEO), including SSO, cover the entire Earth over one to several days, depending on instrument and orbit characteristics. Most aerosol retrieval algorithms have been developed for LEO satellites (Kim et al., 2007; Lyapustin et al., 2011a, b; Lee et al., 2012; Fukuda et al., 2013; Hsu et al., 2013; Levy et al., 2013; Garay et al., 2017, 2020). Instruments currently onboard satellites include the Moderate Resolution Imaging Spectrometer (MODIS), Visible Infrared Imaging Radiometer Suite (VIIRS), Multi-angle Imaging SpectroRadiometer (MISR), and Cloud and Aerosol Imager (CAI) (Remer et al., 2005; Lyapustin et al., 2011a, b, 2018; Fukuda et al., 2013; Hsu et al., 2013; Levy et al., 2013; Garay et al., 2017, 2020).

Representative algorithms developed for MODIS data include the Dark-Target (DT; Remer et al., 2005; Levy et al., 2013), Deep Blue (DB; Hsu et al., 2013; Sayer et al., 2014), and Multi-Angle Implementation of Atmospheric Correction (MAIAC; Lyapustin et al., 2011a, b) systems, which are also applied for the succeeding VIIRS (Sayer et al., 2018). In the DT algorithm, the 2.1 μm channel is used to estimate land-surface reflectance in the visible (VIS) region using empirical equations based on the normalized difference vegetation index (NDVI). The DT algorithm has improved surface-reflectance modelling through consideration of the fractional area of urbanization (Gupta et al., 2016). Ocean-surface reflectance is estimated using the Cox and Munk method (Cox and Munk, 1954), and AOPs over land and ocean are provided at spatial resolutions of 10 km × 10 km and 3 km × 3 km (Remer et al., 2013), respectively. The DB algorithm has an advantage over the DT algorithm in allowing aerosol data retrieval over bright surfaces. By using a shorter-wavelength channel, accuracy is improved over bright surfaces such as urban and desert areas, where surface reflectance was previously estimated by the minimum reflectance method (MRM; Herman and Celarier 1997; Koelemeijer et al., 2003; Hsu et al., 2004). Furthermore, with the improvement to Collection 6.1, land-surface reflectance can be estimated similarly to the DT method, over densely vegetated regions (Sayer et al., 2019). In the case of VIIRS DB, aerosol retrieval over the ocean is also applied by the Satellite Ocean Aerosol Retrieval (SOAR) algorithm (Sayer et al., 2018). In the MODIS MAIAC system, surface reflectance is estimated by considering various images based on time-series analysis, with multi-angle observations, based on up to 16 day data, and by applying the bidirectional reflectance distribution function (BRDF). Ocean-surface reflectance is determined using a Cox and Munk BRDF model similar to DT and VIIRS DB (Lyapustin et al., 2011a, b, 2018). The MISR observes Earth at nine different angles, providing a high degree of freedom in signals; consequently, retrievals yield estimates of aerosol type and shape. As with the MAIAC, multiple observations are used, with the estimation of land-surface reflectance involving bidirectional reflectance factors (BRF). Zhang et al. (2016) developed an aerosol retrieval algorithm that allows aerosol data retrieval over bright land surfaces using surface-reflectance ratios from the VIIRS.

Aerosol retrieval algorithms for geosynchronous Earth orbit (GEO) satellites have been developed, including the Geostationary Operational Environmental Satellite (GOES) series in the USA (Knapp et

https://doi.org/10.5194/amt-2020-336
Preprint. Discussion started: 17 September 2020


Atmospheric Measurement Techniques Discussions

al., 2005), Meteosat series in Europe (Bernard et al., 2011), Himawari series in Japan (Yoon et al., 2007; Kim et al., 2008; Lim et al., 2018; Kikuchi et al., 2018; Yoshida et al., 2018; Gupta et al., 2019), and the Geostationary Korea Multi-Purpose Satellite (GEO-KOMPSAT, GK) series in South Korea (Kim et al., 2014, 2016; Choi et al., 2016, 2018; Kim et al., 2020). However, previously launched geostationary meteorological satellites had only a single, broadband VIS channel, with which it is difficult to retrieve AOPs other than aerosol optical depth (AOD) (Wang et al., 2003; Knapp et al., 2005; Kim et al., 2008, 2014, 2016; Bernard et al., 2011). However, the Geostationary Ocean Color Imager (GOCI) onboard the GK-1 satellite, also known as the Communication, Ocean, and Meteorological Satellite (COMS), has six VIS and two near-infrared (NIR) channels, which is advantageous for retrieving AOPs (Lee et al., 2010; Choi et al., 2016, 2018; Kim et al., 2017). Next-generation meteorological GEO satellite instruments, including the Advanced Himawari Imager (AHI), Advanced Baseline Imager (ABI), and Advanced Meteorological Imager (AMI), have three to four VIS and NIR channels, which enable aerosol property retrieval with high accuracy (Lim et al., 2016, 2018; Kikuchi et al., 2018; Yoshida et al., 2018; Gupta et al., 2019). Kikuchi et al. (2018) and Yoshida et al. (2018) performed aerosol retrievals using the MRM and corrected reflectance using empirical equations. Gupta et al. (2019) extended the MODIS DT algorithm to GEO satellites and estimated visible surface reflectance using SWIR reflectance. Lim et al. (2018) retrieved the AOPs using both MRM and estimated surface reflectance from short-wave IR (SWIR) data (estimated surface reflectance, ESR), and presented the two merged products: an L2-AOD merged product, and a reprocessed AOD produced by merging MRM and ESR surface reflectances.

Algorithms developed to date for LEO and GEO satellites have both advantages and disadvantages, depending on algorithm characteristics. Therefore, the MODIS team provides combined DT and DB AOD products (Levy et al., 2013; Sayer et al., 2014). In addition, several studies of the fusion of L2 products have been conducted (Levy et al., 2013; Sayer et al., 2014; Wei et al., 2019), with Bilal et al. (2017) obtaining reliable results from merged DT and DB products, as indicated by the NDVI in East Asia, and also robust products by simply averaging DT and DB without consideration of the NDVI. AOP data fusion in East Asia may also be achieved using aerosol products of AMI, GOCI-2, and the geostationary environment monitoring spectrometer (GEMS) onboard the GK-2A and 2B satellites launched by South Korea in 2018 and 2020, respectively, with accuracy over bright surfaces being improved by the GEMS aerosol product. It is also possible to obtain accurate AOPs, such as single-scattering albedo, aerosol loading height, and fine-mode fraction, which have been difficult to obtain by fusion of L2 data and/or surface reflectance data. If the trace-gas dataset retrieved from GEMS is used, it is possible to improve the aerosol type, with the retrieval of high-quality AOD data.

Several studies have considered AOD data fusion, for which methods can be broadly classified into two types. First, the fusion of more than one AOD product may involve optimal interpolation (Xue et al., 2012), linear or second-order polynomial functions (Mélin et al., 2007), arithmetic or weighted means (Gupta et al., 2008), or maximum-likelihood estimates (MLE) (Nirala, 2008; Xu et al., 2015; Xie et al., 2018). Second, in the absence of satellite-derived AOD products for the day of fusion, the geostatistical fusion method, universal kriging method (Chatterjee et al., 2010; Li et al., 2014), geostatistical inverse modelling (Wang et al., 2013), or spatial statistical data fusion (Nguyen et al., 2012) may be applied. These have the advantage that AOD can be estimated by integrating the spatial autocorrelation of AOD data even for pixels missing from the AOD products, although there is a

https://doi.org/10.5194/amt-2020-336
Preprint. Discussion started: 17 September 2020


Atmospheric Measurement Techniques Discussions

disadvantage in not considering temporal correlations. The Bayesian maximum entropy (BME) method, taking into account temporal autocorrelation, has also been developed (Tang et al., 2016). BME methodology can estimate gap-filling pixels that are difficult to retrieve due to clouds, but with somewhat reduced accuracy. Gap filled AOD using the BME method, and satellite-derived AOD discontinuity arises from insufficient temporal sampling being available with the use of LEO satellites, resulting in a low fusion synergy.

In this study, the GEO satellite dataset was used to resolve the temporal sampling issue for data fusion, while maintaining the spatio-temporal resolution retrieved from GEO satellites. We also attempted to estimate fused AOD products with higher accuracy in East Asia. The ensemble-mean and MLE methods were applied. Section 2 describes the two algorithms used in this study for AHI and GOCI. Section 3 mentions methods of fusion and systematic bias correction, and section 4 performs validation of the fused products with the Aerosol Robotic Network (AERONET) and Sun-Sky Radiometer Observation Network (SONET) instruments during two field campaigns: the Korea–United States Air Quality Study (KORUS-AQ) and the Effect of Megacities on the Transport and Transformation of Pollutants on Regional and Global Scales Study (EMeRGe).

2. Descriptions of AHI, GOCI, the YAER algorithm, and the two field campaigns

2.1 AHI aerosol algorithm

The Himawari-8 and -9 satellites were launched by the Japanese Meteorological Agency (JMA) on 7 October 2014 and 2 November 2016, respectively. The AHI onboard these satellites has 16 channels covering wavelengths of 0.47–13.3 μm and performs full-disk and Japan-area observations every 10 and 2.5 min, respectively, from GEO at 140.7° E longitude (Bessho et al., 2016). Visible and NIR observations are also performed at high spatial resolutions of 0.5–1.0 km, with SWIR to IR at 2 km, which have advantages in aerosol property retrieval and cloud masking.

Lim et al. (2018) developed the AHI Yonsei aerosol retrieval (YAER) algorithm and provided two retrieval results with 6 km × 6 km resolution based on MRM and ESR using SWIR data. Aerosol property retrieval using VIS channels requires accurate surface reflectance, for which MRM and ESR are useful, with the main difference between the two lying in the surface-reflectance estimation method.

The MRM applies the minimum-reflectance technique over both land and ocean (Lim et al., 2018), with surface reflectance being estimated by finding the minimum reflectance in each pixel over the past 30 day window, giving the Lambertian equivalent reflectance (LER; Knapp et al., 2002; Wang et al., 2003; Kim et al., 2008; Choi et., 2016, 2018; Kim et al., 2016; Lim et al., 2018). This method takes the bidirectional characteristics of surface reflectance into consideration by obtaining surface reflectance at each observation time over the 30-day search window. However, the method assumes that during the search window there is more than one clear day and that surface reflectance does not change; otherwise, it is affected by clouds and/or the background aerosol optical depth (BAOD; Kim et al., 2014).

According to the ESR method, land-surface reflectance in the Vis region is constructed from the Top of Atmosphere (TOA) reflectance at 1.6 μm wavelength, based on the NDVI for SWIR and the fraction of urbanization and cropland (Levy et al 2013; Gupta et al., 2016; Zhong et al., 2016; Lim et al., 2018). Ocean-surface reflectance is estimated from the Cox and Munk BRDF model (Hsu et al., 2004; Lee et

https://doi.org/10.5194/amt-2020-336
Preprint. Discussion started: 17 September 2020


Atmospheric Measurement Techniques Discussions

al., 2012; Jackson et al., 2013; Choi et al., 2016, 2018; Lim et al., 2018; Sayer et al., 2018).
Chlorophyll-a concentrations are considered in addition to data from Japan Aerospace Exploration Agency (JAXA) (Murakami et al., 2016) and interpolated for the 10-min AHI intervals. For unretrieved pixels, the East Asian climatological value of 0.02 mg m^{-3} is used (Yamada et al., 2004). Details of the methodology can be found in Lim et al. (2018).

The MRM gives better accuracy over brighter surfaces such as urban areas, while the ESR method gives better accuracy over areas of dense vegetation (Lim et al., 2018). However, there is a critical surface reflectance at which aerosol signals disappear, depending on the single-scattering albedo (Kim et al., 2016). Over the ocean, both the MRM and ESR methods give high accuracy, but ESR results are robust with the Cox and Munk model.

The MRM requires more computational time than the ESR method to estimate surface reflectance, as it requires data for the past 30 days, and LER needs to be calculated using a radiative transfer model. The ESR method estimates surface reflectance from the observed TOA reflectance at 1.6 μm wavelength using empirical equations including the NDVI. The advantage of MRM is that stable surface reflectance values can be obtained regardless of surface type. However, due to the influence of BAOD, surface reflectance tends to be overestimated, with satellite-derived AOD data thus being underestimated (Kim et al., 2014). On the other hand, the ESR method uses TOA reflectance at 1.6 μm wavelength to detect surface signals, which is less sensitive to fine particles and BAOD. However, when aerosols such as yellow dust with coarse particles are transported from the Taklamakan and Gobi deserts, the BAOD effect also applies to the ESR method. The ESR method is also more likely to be affected by snow surfaces than the MRM, as snow reduces reflectivity around the 1.6 μm wavelength (Negi and Kokhanovsky, 2011). The ESR method also has the disadvantage of giving noisy results over bright surfaces such as desert. However, its fast surface-reflectance estimation enables near-real-time retrieval based on the AHI YAER algorithm.

2.2 GOCI aerosol algorithm

GOCI is an ocean color imager launched onboard COMS in 2010 and observes the East Asia region at an hourly interval with 500 m× 500 m resolution (Choi et al., 2012). It has eight bands in the VIS and NIR regions, which is advantageous for aerosol retrieval. Two versions of GOCI Yonsei aerosol algorithms have been developed, referred to as V1 and V2 (Lee et al., 2010; Choi et al., 2016, 2018). In the case of V1, surface reflectance is estimated by the MRM using LER for the past 30 days over land, and the Cox and Munk BRDF model over oceans. In V2, ocean-surface reflectance is estimated by the same method, but land-surface reflectance is improved by using an accumulated long-term database. To minimize the impact of BAOD (the weakness of the MRM), a monthly surface-reflectance database was constructed using all of the LERs over the past five years, but it cannot reflect unexpected changes in surface conditions. However, a well-established climatological database allows aerosol property retrieval in near-real-time with reasonable accuracy.
Satellite-derived AODs have different error characteristics for NDVI, scattering angle, and so on (Choi et al., 2016, 2018; Lim et al., 2018). Over oceans, ESR AODs are more accurate than MRM values. However, in GOCI, the NDVI shows a negative bias in V1 and positive bias in V2. In this study, we

https://doi.org/10.5194/amt-2020-336
Preprint. Discussion started: 17 September 2020


Atmospheric Measurement Techniques Discussions

developed optimal AOPs in East Asia by fusing two AHI aerosol products from the MRM and ESR methods, and GOCI products from V1 and V2.

2.3 Evaluation of aerosol products during two field campaigns

The performance of fused products was analyzed in two field campaigns: the KORUS-AQ of 1 May 2016 to 12 Jun 2016 (https://www-air.larc.nasa.gov/missions/korus-aq/), and EMeRGe of 12 Mar 2018 to 8 Apr 2018 (https://www.halo.dlr.de/science/missions/emerge/emerge.html). KORUS-AQ was an international multi-organization mission to observe air quality across the Korean Peninsula and surrounding waters, led by the US National Aeronautics and Space Administration (NASA) and the Korean National Institute of Environmental Research (NIER). EMeRGe aimed to investigate experimentally the patterns of atmospheric transport and transformation of pollution plumes originating from Eurasia, tropical and subtropical Asian megacities, and other major population centers. GEO satellite data played an important role in these campaigns; e.g., data assimilation for chemical transport models and tracking aerosol plumes (Saide et al., 2014; Pang et al., 2018; Saide et al., 2020). Here, we applied satellite-derived GOCI and AHI AODs, with a spatial resolution of 6 km × 6 km, and temporal resolutions of 1 hour and 10 minutes, respectively.

3. Data fusion methods

3.1 Spatio-temporal matching

The AHI and GOCI have different spatial pixel locations and temporal resolutions, so it is necessary to match their spatio-temporal resolutions before data fusion. GOCI and AHI AODs have the same spatial resolution of 6 km × 6 km, but the two satellites are located at 128.2° E and 140.7° E, respectively, at the Equator. Spatial pixel matching is therefore required. However, satellite-derived AOD represents total-column extinction, so AOD retrieved by the two sensors is not significantly affected by satellite position. To merge the different satellite spatial pixel coverages, the GOCI pixel was re-gridded to match AHI pixels for full-disk observation, with up to 4 GOCI AOD pixels being used with average values considered representative of pixel values. If more than half of the AHI AOD pixels did not exist out of the maximum 6 AHI data per hour, it is regarded as cloud contaminated pixels and an additional cloud removal process is performed. This process applies to both the MRM and ESR method, to remove the AHI's additional cloud-contaminated pixels in products of both GOCI V1 and V2, which have a disadvantage in cloud masking due to their lack of IR channels. When three or more pixels were available for generating AHI data at 1 hour intervals, hourly AOD values were estimated as the medians of pixel values.

3.2 Ensemble mean method

Here, AMR represents AHI MRM AOD, AES represents AHI ESR AOD, GV1 represents GOCI V1 AOD, and GV2 represents GOCI V2 AOD. We performed data fusion using AMR, AES, GV1, and GV2 data within 1 hour intervals for which additional-cloud masking was performed. The ensemble

https://doi.org/10.5194/amt-2020-336
Preprint. Discussion started: 17 September 2020


Atmospheric Measurement Techniques Discussions

mean is the mean of the ensemble member over a specific time. The ensemble members are AMR, AES, GV1, and GV2 based on two satellite instruments and two different surface-estimation methodologies. Table 1 provides the satellite-derived AOD used for ensemble-mean and MLE fusion.

Fusion was performed only when a pixel of an ensemble member was used for all fusions. Fusion 1 (F1) included the two AHI products of AMR, and AES and GV2. Fusion 2 (F2) involved the calculation of the YAER algorithm by the fusion of AES and GV2, both of which have the advantage of producing data in near-real-time. Fusion 3 (F3) merged AMR and AES to estimate AOD over a wide area, and Fusion 4 (F4) involved a comparison with F1 to determine how accuracy varied with increasing number of ensemble members. FM1 is the result of MLE fusion involving all satellite-derived AOD, and FM2 involves AER and GV2 for near-real-time operation. FM3 includes AMR and AES, enabling wide-area observation.

3.3 MLE method

The MLE method provides a means of weighting and averaging based on errors evaluated with AERONET ground-based measurements (Nirala, 2008; Xu et al., 2015; Xie et al., 2018).

This method employs the following equations:

$$\tau_i^{MLE} = \sum_{k=1}^{N} \frac{R_{i,k}^{-2}}{\sum_{k=1}^{N} R_{i,k}^{-2}} \tau_{i,k} \quad (1)$$

$$R_{i,k} = \sqrt{\frac{\sum_{i=1}^{M} (s_{i,k} - g_i)^2}{M}} \quad (2)$$

where τ_i^{MLE} represents the fused AOD; $\tau_{i,k}$ represents the mean AOD at grid point *i* from the satellite-derived AOD product *k*, where *k* is the index for different satellite-derived AOD products for fusion; $R_{i,k}$ represents the root-mean-square error (RMSE) at grid point *i* for the satellite-derived AOD product *k*; *N* is the number of all AOD data; g_i represents the mean of ground-based AOD at grid point *i* from the AERONET/SONET (collocated temporal mean); $s_{i,k}$ represents the mean of satellite derived AOD products (*k*) at grid points of the AERONET/SONET (collocated spatial mean); and *M* is the number of pairs of $s_{i,k}$ and g_i.

The RMSE used here was calculated by comparing average AERONET/SONET AODs over ±30 minutes intervals with respect to the satellite observation time, and AODs within 25 km of the AERONET/SONET site. For MLE over wide areas without ground measurements, the RMSE was

https://doi.org/10.5194/amt-2020-336
Preprint. Discussion started: 17 September 2020


Atmospheric Measurement Techniques Discussions

estimated by grouping AODs based on NDVI bins; their values for the KORUS-AQ period are summarized in Table 2. We excluded points that were >2 standard deviations (SD) to remove outliers and to consider only the more stable RMSE values.

3.4 Bias correction

AOD follows a log-normal distribution (Sayer et al., 2013), but AOD differences with respect to AERONET/SONET data (dAOD) for each satellite product follow a Gaussian distribution. The error distributions of AMR, AESR, GV1, and GV2 used here also follow a Gaussian distribution, with dAOD during the KORUS-AQ and EMerGe campaigns being as shown in Figure 1. To minimize the effect of outliers in this process, data beyond 2 SD were excluded and applied differently according to NDVI and time. Data beyond 2 SD of dAOD were excluded to prevent a change in bias trends due to AOD errors caused by cloud shadows and pixels contaminated by clouds. Bias correction values are provided in Table 3. This process was performed before applying the MLE method, which allows compensation for systematic bias that is difficult to obtain directly in MLE.

4. Results

AOD products retrieved by each satellite instrument, ensemble-mean products, and the fusion products of the MLE method, are shown in Figure 2 for the KORUS-AQ period and in Figure 3 for the EMeRGe period. The AOD fusion products (Figure 2a–d) tends to indicate higher AODs on the western side of the Korean Peninsula than the eastern side, and high AODs in Hokkaido, Japan. The same trends are observed over China with high AODs, where the AER product shows the highest values, and the respective satellite products display similar patterns. Large differences are evident in southern Tibet and the Taklamakan desert (Figure 2a, b) as a result of the error in the ESR method caused by unreliable surface reflectance over bright surfaces resulting in overestimation of AOD, as reported in previous studies (Levy et al., 2013; Gupta et al., 2016). The aerosol spatial distribution (Figure 2e–h) is similar in the different satellite products, and smooth overall. High AODs are noticeable over Shanghai, Hong Kong, and Hanoi (Figure 2g), consistent with the results of previous studies that reported high concentrations of surface particulate matter in urban regions. MLE results (Figure 2i–k) are similar to the ensemble-mean products. Results for the EMeRGe campaign (Figure 3) are similar to those in Figure 2, but with higher AODs in northwestern Japan, Hokkaido, and northern Russia (particularly in Figure 3b). The AMR product (Figure 3a, c, d) indicates small errors, but snow masking needs to be improved. It also shows high AODs over the Yellow Sea, indicating that aerosols were transported from China during the EMeRGe campaign. For the ensemble mean AODs, each satellite-derived product complements each other, reduced the scattered distribution in the lower AOD region to improve overall accuracy which can be compared and demonstrated well at sites with low aerosol loadings in particular.

The Gangneung-Wonju National University site (Gangneung-WNU; 128.87°E, 37.77°N) lies on the eastern side of the Korean Peninsula and it is one of the regions with low aerosol loadings. The AOD frequency distribution generally follows a log-normal distribution, and it is important to estimate low

https://doi.org/10.5194/amt-2020-336
Preprint. Discussion started: 17 September 2020


Atmospheric Measurement Techniques Discussions

AOD levels exactly to increase its accuracy. Therefore, we evaluated whether the fused and MLE products were improved at low AODs. A time-series comparison of different satellite AOD products with AERONET (on a logarithmic scale) is shown in Figure 4 for the Gangneung-WNU site without high AOD events, where most point AERONET AODs at 550 nm were < 1 during the KORUS-AQ campaign. Time-series data from ground instrument, AMR, AES, GV1, and GV2 products are shown in Figure 4a, where black filled circles represent AERONET AOD as ground-truth data, and satellite-derived AODs (in different colors) display similar variabilities. AMR, GV1, and GV2 outputs based on the MRM generally exhibit negative biases, with AES AODs being higher than other products. Ensemble-mean and MLE results are presented in Figure 4b and c, respectively, and show better agreement with the AERONET AOD than individual satellite AODs. MLE results, which consider pixel-level uncertainties (in contrast to ensemble means), are superior in following the variability of ground-based AERONET observations, even at low AODs. The MLE products were implemented in a way to improve accuracy for the low AOD region more critically than in the high AOD region by systematic bias correction. Surface reflectance estimated by the MRM is affected by BAOD, and AOD thus shows a negative bias. On the other hand, the AER uses TOA reflectance at 1.6 μm wavelength to estimate surface reflectance and is therefore less affected by BAOD, and shows higher AOD than AMR and the two GOCI AODs. Furthermore, AOD retrieval over vegetated areas is more accurate with the ESR method. This result is consistent with previous studies of aerosol retrieval in the VIS region (Levy et al., 2013; Gupta et al., 2019; Hsu et al., 2019).

5. Error estimation and validation against AERONET and SONET

For validation and error estimation, AERONET/SONET aerosol products were used for ground truth. AERONET/SONET offers freely available spectral AOD measurements every 15 min (or less) at numerous monitoring sites worldwide, with an uncertainty of 1%–2% under cloudless conditions (Smirnov et al., 2000; Holben et al., 2001). Newly updated AERONET Version 3 Level 2.0 AOPs with additional cloud screening and quality control were selected for validation purposes (Giles et al., 2019). The number of AERONET/SONET sites used for validation in this study, was 78 and 42 during the KORUS-AQ campaign, and 68 and 27 during the EMeRGe campaign, for AHI and GOCI, respectively.

5.1 Validation with AERONET and SONET

Spatio-temporal correlation between satellite-derived AOD and AERONET/SONET AOD involved data averaged over all satellite pixels within a 25 km radius of the AERONET/SONET site, and AERONET/SONET AOD averaged over ±30 minutes from the satellite observation time. As validation metrics, Pearson's correlation coefficient, mean absolute error (MAE), median bias error (MBE), and the fraction (%) within the expected error (EE) were applied. The MODIS DT algorithm provided EE as $\pm 0.05 \pm 0.15 \times$ AOD (Levy et al., 2010). Results of the comparison with AERONET during KORUS AQ are shown in Figure 5, the EE values of AER, AES, G1, and GV2 were 53.1%, 58.5%, 51.0%, and 49.0%, respectively. Fused products and MLE products have EE values of up to 71.9%, much higher

https://doi.org/10.5194/amt-2020-336
Preprint. Discussion started: 17 September 2020


Atmospheric Measurement Techniques Discussions

than the respective satellite product. In terms of RMSE, the fusion products have a value of 0.131, lower than the minimum value of various satellite products (0.161). Figure 5g and k shows relatively scattered patterns compared with other fusion products because they show data fused with only AHI products. EE values for all AERONET products used for validation are shown in Figure 6, where AHI covers a broader area than GOCI. The accuracy is low over northern India and the Indochina Peninsula. However, EE values after fusion (Figure 6g, k) are higher than those of the respective satellite product. The fused results (Figure 6g, k) of only two AHI products display high EE values within the domains of GOCI and other fusion products. The scattered fusion results based on two AHI products (Figure 5) can thus be attributed to issues at these particular sites, rather than to the satellite products themselves. Results of the comparative validation with AERONET during the EMeRGe campaign (Figure 7) indicate that, overall, fusion products improve the statistical metrics, as in the KORUS-AQ case. The validation result for each satellite product shows that the maximum value of EE is 61.5%–68.9% after fusion. Thus, the EE increases as other statistics improve, including an RMSE decrease from 0.167 to 0.146, and an MBE decrease to zero.

As in the KORUS-AQ campaign, the validation results for the two AHI products and the fusion products based on AHI AODs only are inferior to the results for the fusion products based on GOCI AODs. This is because the validation was performed over wider areas, and problems were noted at specific sites. The fused results showed improved accuracy not only in terms of EE but also in statistical metrics such as RSME, MBE, and MAE. Results for the EMeRGe campaign are shown in Figure 8. During that campaign, validation results over brighter surfaces in northern India and the Indochina Peninsula show reduced accuracy, but fusion results show consistently higher EE values than individual satellite products.

5.2 Error estimation

Differences between satellite products and AERONET, dAOD values were analyzed on the basis of NDVI values and observation times (Figure 9). Figure 9a and d shows the respective satellite products, Figure 9b and c the ensemble-mean product, and Figure 9c and f the MLE fusion results, with each filled circle representing the mean of 800 and 600 collocated data points sorted in terms of NDVI for the KORUS-AQ and EMeRGe campaigns, respectively. Figure 9a shows different biases for each satellite product, with AMR and GV1 being negative, AES positive, and GV2 converging to almost zero. The errors are close to zero for both the ensemble-mean and MLE products as a result of the fusion process. During the EMeRGe campaign (right column, Figure 9), the two AHI and two GOCI products show negative biases, and even the ensemble-mean results have negative biases. The ensemble mean does not include any bias correction, meaning that the error characteristics of each original satellite product are intact. The MLE products display improved biases in terms of NDVI, which are close to zero because the bias was corrected for in the MLE process.

The mean bias of the AOD products over the observation time was analyzed as shown in Figure 10 where, as in Figure 9, the left column represents the KORUS-AQ and the right column the EMeRGe campaign, with filled circles representing mean values, and the error bar being ±1 SD. As in Figure 9, the AMR displays a generally negative bias, as in the all-time results, and a negative bias also exists in each time zone. However, the AES shows a positive bias. In the GOCI case, positive and negative

https://doi.org/10.5194/amt-2020-336
Preprint. Discussion started: 17 September 2020


Atmospheric Measurement Techniques Discussions

biases appear differently according to time zones. In the EMeRGe period, the two AHI results have large error ranges. GEO satellites perform observations over a specific area with a fixed viewing zenith-angle and retrieve AOPs by solar reflectance, which means that a specific site has different local time depending on its longitude for a given satellite image. Furthermore, there are fewer data for the EMeRGe period than the KORUS-AQ period, and data for northern India and the Indochina Peninsula, which have low accuracy, are included in the data for 0100–0300 UTC, indicating large errors. In the KORUS-AQ period, the data fraction for a specific site is not as large as in the EMeRGe period, so this problem does not arise. Taylor diagrams for accuracy evaluation of AOD data fusion products are shown in Figure 11. The Taylor diagram is a graphic summary of how closely satellite retrievals match observations. Here, match-up values were respective and fusion AOD products, and the matching up data were AERONET AOD. Correlation coefficient, SD, RSME, and EE values were used as the matching criteria. The correlation coefficient is shown in green (Figure 11) with a polar angle, the SD is shown in the radial distance on the black x- and y-axes, and RMSE is the proportional cyan circle from the "AERONET" point on the x-axis. The EE value, which can evaluate the stability of AODs, is shown for each color. All open symbols represent the results of selecting only the same collocation site as GOCI, and the filled symbols are comparative validations of all sites. GV1, GV2, AMR, AES, F1, F2, F3, F4, FM1, FM2, and FM3 are indicated by diamond, star, square, circle, top half-circle, lower half-circle, left half-circle, right half-circle, down-pointing triangle, right-pointing triangle, and left-pointing triangle shapes, respectively.

The filled symbols cover a large area, so sites with poor accuracy are reflected in correlations, SD, RMSE, and EE values. Correlation coefficients are all around 0.8–0.9 with no significant differences for respective and fusion AODs. However, results after fusion show slightly better than respective satellite product accuracy in terms of SD, RMSE, and EE values.

Standard deviation values indicate that products that lie outside the purple dotted half-circle are larger than the SD of AERONET. In the AHI case, the SD appears smaller than GOCI values because it tends to underestimate values at high AOD. Similarly, RMSE values are lower after fusion. However, the results of AMR and AER included in the GOCI observation area show better accuracy than the GOCI, with statistical metrics similar to those of the fusion products.

The EMeRGe period was from March to April, when the surface is brighter in East Asia than during the KORUS-AQ period of May to June. The accuracy during the EMeRGe period is therefore similar to or slightly poorer than that of the KORUS-AQ period. The correlation coefficient shows similar values, but the SD, RMSE, and EE values are slightly lower. Again, the accuracy of the validation metrics is improved by fusion.

The error analysis indicates that the results after fusion are more accurate than the results obtained using individual satellite product, and accuracy was slightly better during KORUS-AQ than EMeRGe because more data points were considered.

https://doi.org/10.5194/amt-2020-336
Preprint. Discussion started: 17 September 2020


Atmospheric Measurement Techniques Discussions

6. Summary and conclusion

Various aerosol algorithms have been developed based on two different GEO satellites, AHI, and GOCI. Retrieved AOD data have advantages and disadvantages, depending on the concept of the algorithm and surface-reflectance estimations. In this study, four aerosol products (GV1, GV2, AMR, and AES) were used to construct ensemble-mean and MLE products. Based on the ensemble mean, this study presented fusion products taking advantage of overlap region, accuracy, and near-real-time processing, as well as MLE products including pixel-level errors. Bias corrections for different times were performed while considering pixel-level errors, and the synergy of fusion between GEO satellites demonstrated.

Validation with the AERONET confirmed that consideration of pixel-level uncertainty improved the accuracy of MLE products. The accuracy after fusion was better than that of individual satellite product. The EE of each satellite-derived product during the KORUS-AQ was 53.1%, 58.5%, 51.6%, and 49.0% in AMR, AES, GV1, and GV2; and the RMSE was 0.179, 0.197, 0.161, and 0.183, respectively. After the ensemble-mean process, the EE of F1, F2, F3, and F4 increased to 71.9%, 71.4%, 63.9%, and 66.5%, respectively. FM1, FM2, and FM3, which are results of MLE fusion, had EE values of 69.0%, 63.8%, and 59.2%, with RMSE values of 0.137, 0.150, and 0.168, respectively, better than the respective satellite product. Similarly, the EMeRGe period displayed better statistical values after fusion, with EE and RMSE values of 68.9% and 0.146, respectively. Error was reduced for bias due to NDVI, scattering angle, and time, to provide optimized AOD products for East Asia. However, since both satellite algorithms retrieved AOPs through VIS channels, there remains an issue of reduced accuracy over brighter surfaces, with AOP retrieval in the VIS channel being more accurate over dark surfaces, and with results being more accurate during the KORUS-AQ period than the EMeRGe period. The fusion products improved the accuracy of satellite products, and MLE products further improved the accuracy by taking into account pixel-based errors based on long-term data analysis. The method applied in this study could be used for AOD fusion of GEO data, such as GK-2A and 2B. Furthermore, it is possible to retrieve AOPs other than AOD using multi-angle, multi-channel (UV, VIS, and IR) observations with GK-2A and 2B.

Code and data availability.

The aerosol products data from AHI and GOCI are available on request from the corresponding author (jkim2@yonsei.ac.kr).

Author contributions.

HL, SG and JK designed the experiment. HL and SG carried out the data processing. MC, SL, and YK provided support on satellite data. HL wrote the manuscript with contributions from co-authors. JK reviewed and edited the article. JK and CK provided support and supervision. All authors analyzed the measurement data and prepared the article with contributions from all co-authors.

https://doi.org/10.5194/amt-2020-336
Preprint. Discussion started: 17 September 2020

Atmospheric Measurement Techniques Discussions

Competing interests.

The authors declare that they have no conflict of interest.

Acknowledgements

This subject is supported by Korea Ministry of Environment (MOE) as "Public Technology Program based on Environmental Policy (2017000160001)". This work was also supported by a grant from the National Institute of Environment Research (NIER), funded by the Ministry of Environment (MOE) of the Republic of Korea (NIER-2020-01-02-007). This research was also supported by the National Strategic Project-Fine particle of the National Research Foundation of Korea(NRF) funded by the Ministry of Science and ICT(MSIT), the Ministry of Environment(ME), and the Ministry of Health and Welfare(MOHW) (NRF-2017M3D8A1092022). We thank all members of the KORUS-AQ science team for their contributions to the field study and the data processing (doi:10.5067/Suborbital/KORUSAQ/DATA01).

References

Bernard, E., Moulin, C., Ramon, D., Jolivet, D., Riedi, J., and Nicolas, J. M.: Description and validation of an AOT product over land at the 0.6 µm channel of the SEVIRI sensor onboard MSG, Atmospheric Measurement Techniques, 4, 2543-2565, 2011.

Bessho, K., Date, K., Hayashi, M., Ikeda, A., Imai, T., Inoue, H., Kumagai, Y., Miyakawa, T., Murata, H., Ohno, T., Okuyama, A., Oyama, R., Sasaki, Y., Shimazu, Y., Shimoji, K., Sumida, Y., Suzuki, M., Taniguchi, H., Tsuchiyama, H., Uesawa, D., Yokota, H., and Yoshida, R.: An Introduction to Himawari-8/9— Japan’s New-Generation Geostationary Meteorological Satellites, Journal of the Meteorological Society of Japan. Ser. II, 94, 151-183, 2016.

Bilal, M., Nichol, J. E., and Wang, L.: New customized methods for improvement of the MODIS C6 Dark Target and Deep Blue merged aerosol product, Remote Sensing of Environment, 197, 115-124, 2017.

Chatterjee, A., Michalak, A. M., Kahn, R. A., Paradise, S. R., Braverman, A. J., and Miller, C. E.: A geostatistical data fusion technique for merging remote sensing and ground-based observations of aerosol optical thickness, Journal of Geophysical Research, 115, 2010.

Cho, Hi K., Jeong, M. J., Kim, J., Kim, Y. J.: Dependence of diffuse photosynthetically active solar irradiance on total optical depth, Journal of Geophysical Research, 108, D9, 4267, 4-1~4-10, 2003.

Choi, J.-K., Park, Y. J., Ahn, J. H., Lim, H.-S., Eom, J., and Ryu, J.-H.: GOCI, the world's first geostationary ocean color observation satellite, for the monitoring of temporal variability in coastal water turbidity, Journal of Geophysical Research: Oceans, 117, C9, 2012.

Choi, M., Kim, J., Lee, J., Kim, M., Park, Y.-J., Jeong, U., Kim, W., Hong, H., Holben, B. N., Eck, T. F., Song, C. H., Lim, J.-H., and Song, C.-K.: GOCI Yonsei Aerosol Retrieval (YAER) algorithm and validation during the DRAGON-NE Asia 2012 campaign, Atmos. Meas. Tech., 9, 1377-1398, 2016.

https://doi.org/10.5194/amt-2020-336
Preprint. Discussion started: 17 September 2020

Choi, M., Kim, J., Lee, J., Kim, M., Park, Y.-J., Holben, B., Eck, T. F., Li, Z., and Song, C. H.: GOCI Yonsei aerosol retrieval version 2 products: an improved algorithm and error analysis with uncertainty estimation from 5-year validation over East Asia, Atmospheric Measurement Techniques, 11, 385-408, 2018.

Cox, C.: Statistics of the sea surface derived from sun glitter, J. Marine Research, 13, 198-227, 1954.

Fukuda, S., Nakajima, T., Takenaka, H., Higurashi, A., Kikuchi, N., Nakajima, T. Y., and Ishida, H.: New approaches to removing cloud shadows and evaluating the 380 nm surface reflectance for improved aerosol optical thickness retrievals from the GOSAT/TANSO-Cloud and Aerosol Imager, Journal of Geophysical Research: Atmospheres, 118, 13,520-513,531, 2013.

Garay, M. J., Kalashnikova, O. V., and Bull, M. A.: Development and assessment of a higher-spatial-resolution (4.4 km) MISR aerosol optical depth product using AERONET-DRAGON data, Atmospheric Chemistry and Physics, 17, 5095-5106, 2017.

Garay, M. J., Witek, M. L., Kahn, R. A., Seidel, F. C., Limbacher, J. A., Bull, M. A., Diner, D. J., Hansen, E. G., Kalashnikova, O. V., Lee, H., Nastan, A. M., and Yu, Y.: Introducing the 4.4 km spatial resolution Multi-Angle Imaging SpectroRadiometer (MISR) aerosol product, Atmospheric Measurement Techniques, 13, 593-628, 2020.

Giles, D. M., Sinyuk, A., Sorokin, M. S., Schafer, J. S., Smirnov, A., Slutsker, I., Eck, T. F., Holben, B. N., Lewis, J., Campbell, J., Welton, E. J., Korkin, S., and Lyapustin, A.: Advancements in the Aerosol Robotic Network (AERONET) Version 3 Database – Automated Near Real-Time Quality Control Algorithm with Improved Cloud Screening for Sun Photometer Aerosol Optical Depth (AOD) Measurements, Atmos. Meas. Tech. Discuss., doi: https://doi.org/10.5194/amt-2018-272, 2018. 2018.

Gupta, P., Patadia, F., and Christopher, S. A.: Multisensor Data Product Fusion for Aerosol Research, IEEE Transactions on Geoscience and Remote Sensing, 46, 1407-1415, 2008.

Gupta, P., Levy, R. C., Mattoo, S., Remer, L. A., and Munchak, L. A.: A surface reflectance scheme for retrieving aerosol optical depth over urban surfaces in MODIS Dark Target retrieval algorithm, Atmospheric Measurement Techniques, 9, 3293-3308, 2016.

Gupta, P., Levy, R. C., Mattoo, S., Remer, L. A., Holz, R. E., and Heidinger, A. K.: Applying the Dark Target aerosol algorithm with Advanced Himawari Imager observations during the KORUS-AQ field campaign, 2019. 2019.

Herman, J., Bhartia, P., Torres, O., Hsu, C., Seftor, C., and Celarier, E.: Global distribution of UV-absorbing aerosols from Nimbus 7/TOMS data, Journal of Geophysical Research: Atmospheres, 102, 16911-16922, 1997.

Holben, B. N., Tanre, D., Smirnov, A., Eck, T., Slutsker, I., Abuhassan, N., Newcomb, W., Schafer, J., Chatenet, B., and Lavenu, F. J. J. o. G. R. A.: An emerging ground-based aerosol climatology: Aerosol optical depth from AERONET, 106, 12067-12097, 2001.

Hsu, N. C., Tsay, S.-C., King, M. D., Herman, J. R. J. I. T. o. G., and Sensing, R.: Aerosol properties over bright-reflecting source regions, 42, 557-569, 2004.

Hsu, N., Jeong, M. J., Bettenhausen, C., Sayer, A., Hansell, R., Seftor, C., Huang, J., and Tsay, S. C.: Enhanced Deep Blue aerosol retrieval algorithm: The second generation, Journal of Geophysical Research: Atmospheres, 118, 9296-9315, 2013.

Hsu, N., Lee, J., Sayer, A., Kim, W., Bettenhausen, C., and Tsay, S. C. J. J. o. G. R. A.: VIIRS Deep Blue aerosol products over land: Extending the EOS long-term aerosol data records, 124, 4026-4053, 2019.

https://doi.org/10.5194/amt-2020-336
Preprint. Discussion started: 17 September 2020


Atmospheric Measurement Techniques Discussions

Jackson, J. M., Liu, H., Laszlo, I., Kondragunta, S., Remer, L. A., Huang, J., and Huang, H.-C.: Suomi-NPP VIIRS aerosol algorithms and data products, Journal of Geophysical Research: Atmospheres, 118, 12,673-612,689, 2013.

Kikuchi, M., Murakami, H., Suzuki, K., Nagao, T. M., and Higurashi, A.: Improved Hourly Estimates of Aerosol Optical Thickness Using Spatiotemporal Variability Derived From Himawari-8 Geostationary Satellite, IEEE Transactions on Geoscience and Remote Sensing, 56, 3442-3455, 2018.

Kim, J., Lee, J., Lee, H. C., Higurashi, A., Takemura, T., and Song, C. H., Consistency of the aerosol type classification from satellite remote sensing during the Atmospheric Brown Cloud–East Asia Regional Experiment campaign, J. Geophys. Res., 112, D22S33, doi:10.1029/2006JD008201, 2007.

Kim, J., Yoon, J. M., Ahn, M. H., Sohn, B. J., and Lim, H. S.: Retrieving aerosol optical depth using visible and mid-IR channels from geostationary satellite MTSAT-1R, International Journal of Remote Sensing, 29, 6181-6192, 2008.

Kim, J., Kim, M., and Choi, M.: Monitoring aerosol properties in east Asia from geostationary orbit: GOCI, MI and GEMS. In: Air Pollution in Eastern Asia: An Integrated Perspective, Springer, 2017.

Kim, J., Jeong, U., Ahn, M.-H., Kim, J. H., Park, R. J., Lee, H., Song, C. H., Choi, Y.-S., Lee, K.-H., Yoo, J.-M., Jeong, M.-J., Park, S. K., Lee, K.-M., Song, C.-K., Kim, S.-W., Kim, Y. J., Kim, S.-W., Kim, M., Go, S., Liu, X., Chance, K., Chan Miller, C., Al-Saadi, J., Veihelmann, B., Bhartia, P. K., Torres, O., Abad, G. G., Haffner, D. P., Ko, D. H., Lee, S. H., Woo, J.-H., Chong, H., Park, S. S., Nicks, D., Choi, W. J., Moon, K.-J., Cho, A., Yoon, J., Kim, S.-k., Hong, H., Lee, K., Lee, H., Lee, S., Choi, M., Veefkind, P., Levelt, P. F., Edwards, D. P., Kang, M., Eo, M., Bak, J., Baek, K., Kwon, H.-A., Yang, J., Park, J., Han, K. M., Kim, B.-R., Shin, H.-W., Choi, H., Lee, E., Chong, J., Cha, Y., Koo, J.-H., Irie, H., Hayashida, S., Kasai, Y., Kanaya, Y., Liu, C., Lin, J., Crawford, J. H., Carmichael, G. R., Newchurch, M. J., Lefer, B. L., Herman, J. R., Swap, R. J., Lau, A. K. H., Kurosu, T. P., Jaross, G., Ahlers, B., Dobber, M., McElroy, C. T., and Choi, Y.: New Era of Air Quality Monitoring from Space: Geostationary Environment Monitoring Spectrometer (GEMS), Bulletin of the American Meteorological Society, 101, E1-E22, 2020.

Kim, M., Kim, J., Wong, M. S., Yoon, J., Lee, J., Wu, D., Chan, P. W., Nichol, J. E., Chung, C.-Y., and Ou, M.-L.: Improvement of aerosol optical depth retrieval over Hong Kong from a geostationary meteorological satellite using critical reflectance with background optical depth correction, Remote Sensing of Environment, 142, 176-187, 2014.

Kim, M., Kim, J., Jeong, U., Kim, W., Hong, H., Holben, B., Eck, T. F., Lim, J. H., Song, C. K., Lee, S., and Chung, C. Y.: Aerosol optical properties derived from the DRAGON-NE Asia campaign, and implications for a single-channel algorithm to retrieve aerosol optical depth in spring from Meteorological Imager (MI) on-board the Communication, Ocean, and Meteorological Satellite (COMS), Atmos. Chem. Phys., 16, 1789-1808, 2016.

Knapp, K. R. J. J. o. G. R. A.: Quantification of aerosol signal in GOES 8 visible imagery over the United States, 107, AAC 4-1-AAC 4-11, 2002.

Knapp, K. R., Frouin, R., Kondragunta, S., and Prados, A.: Toward aerosol optical depth retrievals over land from GOES visible radiances: determining surface reflectance, International Journal of Remote Sensing, 26, 4097-4116, 2007.

Koelemeijer, R., De Haan, J., and Stammes, P.: A database of spectral surface reflectivity in the range 335–772 nm derived from 5.5 years of GOME observations, Journal of Geophysical Research: Atmospheres, 108, 2003.

Lee, J., Kim, J., Song, C. H., Ryu, J.-H., Ahn, Y.-H., and Song, C.: Algorithm for retrieval of aerosol optical properties over the ocean from the Geostationary Ocean Color Imager, Remote Sensing of Environment, 114, 1077-1088, 2010.

Lee, J., Kim, J., Yang, P., and Hsu, N. C.: Improvement of aerosol optical depth retrieval from MODIS spectral reflectance over the global ocean using new aerosol models archived from AERONET inversion data and tri-axial ellipsoidal dust database, Atmospheric Chemistry and Physics, 12, 7087-7102, 2012.

https://doi.org/10.5194/amt-2020-336
Preprint. Discussion started: 17 September 2020

Levy, R. C., Remer, L. A., Kleidman, R. G., Mattoo, S., Ichoku, C., Kahn, R., and Eck, T. F.: Global evaluation of the Collection 5 MODIS dark-target aerosol products over land, Atmospheric Chemistry and Physics, 10, 10399-10420, 2010.

Levy, R. C., Mattoo, S., Munchak, L. A., Remer, L. A., Sayer, A. M., Patadia, F., and Hsu, N. C.: The Collection 6 MODIS aerosol products over land and ocean, Atmospheric Measurement Techniques, 6, 2989-3034, 2013.

Li, L., Shi, R., Zhang, L., Zhang, J., and Gao, W.: The data fusion of aerosol optical thickness using universal kriging and stepwise regression in East China, 2014, 922112.

Lim, H., Choi, M., Kim, M., Kim, J., and Chan, P. W.: Retrieval and Validation of Aerosol Optical Properties Using Japanese Next Generation Meteorological Satellite, Himawari-8, Korean Journal of Remote Sensing, 32, 681-691, 2016.

Lim, H., Choi, M., Kim, J., Kasai, Y., and Chan, P.: AHI/Himawari-8 Yonsei Aerosol Retrieval (YAER): Algorithm, Validation and Merged Products, Remote Sens., 10, 2018.

Lyapustin, A., Martonchik, J., Wang, Y., Laszlo, I., and Korkin, S.: Multiangle implementation of atmospheric correction (MAIAC): 1. Radiative transfer basis and look-up tables, Journal of Geophysical Research, 116, 2011a.

Lyapustin, A., Wang, Y., Laszlo, I., Kahn, R., Korkin, S., Remer, L., Levy, R., and Reid, J. S.: Multiangle implementation of atmospheric correction (MAIAC): 2. Aerosol algorithm, Journal of Geophysical Research, 116, 2011b.

Lyapustin, A., Wang, Y., Korkin, S., and Huang, D.: MODIS Collection 6 MAIAC algorithm, Atmospheric Measurement Techniques, 11, 5741-5765, 2018.

Mélin, F., Zibordi, G., and Djavidnia, S.: Development and validation of a technique for merging satellite derived aerosol optical depth from SeaWiFS and MODIS, Remote Sensing of Environment, 108, 436-450, 2007.

Murakami, H.: Ocean color estimation by Himawari-8/AHI, 2016, 987810.

Negi, H. and Kokhanovsky, A. J. T. C.: Retrieval of snow albedo and grain size using reflectance measurements in Himalayan basin, 5, 203, 2011.

Nguyen, H., Cressie, N., and Braverman, A.: Spatial Statistical Data Fusion for Remote Sensing Applications, Journal of the American Statistical Association, 107, 1004-1018, 2012.

Nirala, M.: Technical Note: Multi-sensor data fusion of aerosol optical thickness, International Journal of Remote Sensing, 29, 2127-2136, 2008.

Pang, J., Liu, Z., Wang, X., Bresch, J., Ban, J., Chen, D., and Kim, J.: Assimilating AOD retrievals from GOCI and VIIRS to forecast surface PM2.5 episodes over Eastern China, Atmospheric Environment, 179, 288-304, 2018.

Remer, L. A., Kaufman, Y., Tanré, D., Mattoo, S., Chu, D., Martins, J. V., Li, R.-R., Ichoku, C., Levy, R., and Kleidman, R.: The MODIS aerosol algorithm, products, and validation, Journal of the atmospheric sciences, 62, 947-973, 2005.

Remer, L. A., Mattoo, S., Levy, R. C., and Munchak, L.: MODIS 3 km aerosol product: algorithm and global perspective, Atmospheric Measurement Techniques Discussions, 6, 69-112, 2013.

Saide, P. E., Kim, J., Song, C. H., Choi, M., Cheng, Y., and Carmichael, G. R.: Assimilation of next generation geostationary aerosol optical depth retrievals to improve air quality simulations, Geophysical Research Letters, 41, 9188-9196, 2014.

Saide, P. E., Gao, M., Lu, Z., Goldberg, D., Streets, D. G., Woo, J.-H., Beyersdorf, A., Corr, C. A., Thornhill, K. L., Anderson, B., Hair, J. W., Nehrir, A. R., Diskin, G. S., Jimenez, J. L., Nault, B. A., Campuzano-Jost, P., Dibb, J., Heim, E., Lamb, K. D., Schwarz, J. P., Perring, A. E., Kim, J., Choi, M., Holben, B., Pfister, G., Hodzic, A., Carmichael, G. R.,

https://doi.org/10.5194/amt-2020-336
Preprint. Discussion started: 17 September 2020

Atmospheric Measurement Techniques Discussions

Emmons, L., and Crawford, J. H. : Understanding and improving model representation of aerosol optical properties for a Chinese haze event measured during KORUS-AQ, Atmospheric Chemistry and Physics, 20, 6455-6478,2020.

Sayer, A. M., Hsu, N. C., Bettenhausen, C., and Jeong, M. J.: Validation and uncertainty estimates for MODIS Collection 6 "Deep Blue" aerosol data, Journal of Geophysical Research: Atmospheres, 118, 7864-7872, 2013.

Sayer, A., Munchak, L., Hsu, N., Levy, R., Bettenhausen, C., and Jeong, M. J.: MODIS Collection 6 aerosol products: Comparison between Aqua's e-Deep Blue, Dark Target, and "merged" data sets, and usage recommendations, Journal of Geophysical Research: Atmospheres, 119, 2014.

Sayer, A., Hsu, N., Lee, J., Bettenhausen, C., Kim, W., and Smirnov, A. J. J. o. G. R. A.: Satellite Ocean Aerosol Retrieval (SOAR) Algorithm Extension to S-NPP VIIRS as Part of the "Deep Blue" Aerosol Project, 123, 380-400, 2018.

Sayer, A. M., Hsu, N. C., Lee, J., Kim, W. V., and Dutcher, S. T.: Validation, Stability, and Consistency of MODIS Collection 6.1 and VIIRS Version 1 Deep Blue Aerosol Data Over Land, Journal of Geophysical Research: Atmospheres, 124, 4658-4688, 2019.

Smirnov, A., Holben, B. N., Eck, T. F., Dubovik, O., and Slutsker, I.: Cloud screening and quality control algorithms for the AERONET data base, Remote Sens. Environ., 73, 337-349, 2000.

Stocker, T. F., Qin, D., Plattner, G.-K., Tignor, M., Allen, S. K., Boschung, J., Nauels, A., Xia, Y., Bex, B., and Midgley, B.: IPCC, 2013: climate change 2013: the physical science basis. Contribution of working group I to the fifth assessment report of the intergovernmental panel on climate change. Cambridge University Press, 2013.

Tang, Q., Bo, Y., and Zhu, Y.: Spatiotemporal fusion of multiple-satellite aerosol optical depth (AOD) products using Bayesian maximum entropy method, Journal of Geophysical Research: Atmospheres, 121, 4034-4048, 2016.

Wang, J.: Geostationary satellite retrievals of aerosol optical thickness during ACE-Asia, Journal of Geophysical Research, 108, 2003.

Wang, J., Brown, D. G., and Hammerling, D.: Geostatistical inverse modeling for super-resolution mapping of continuous spatial processes, Remote Sensing of Environment, 139, 205-215, 2013.

Wei, J., Li, Z., Sun, L., Peng, Y., Zhang, Z., Li, Z., Su, T., Feng, L., Cai, Z., and Wu, H.: Evaluation and uncertainty estimate of next-generation geostationary meteorological Himawari-8/AHI aerosol products, Sci Total Environ, 692, 879-891, 2019.

Xie, Y., Xue, Y., Che, Y., Guang, J., Mei, L., Voorhis, D., Fan, C., She, L., Xu, H. J. I. T. o. G., and Sensing, R.: Ensemble of ESA/AATSR aerosol optical depth products based on the likelihood estimate method with uncertainties, 56, 997-1007, 2017.

Xu, H., Guang, J., Xue, Y., De Leeuw, G., Che, Y., Guo, J., He, X., and Wang, T. J. A. E.: A consistent aerosol optical depth (AOD) dataset over mainland China by integration of several AOD products, 114, 48-56, 2015.

Xue, Y., Xu, H., Mei, L., Guang, J., Guo, J., Li, Y., Hou, T., Li, C., Yang, L., He, X. J. A. C., and Discussions, P.: Merging aerosol optical depth data from multiple satellite missions to view agricultural biomass burning in Central and East China, 12, 10461-10492, 2012.

Yamada, K., Ishizaka, J., Yoo, S., Kim, H.-c., and Chiba, S.: Seasonal and interannual variability of sea surface chlorophyll a concentration in the Japan/East Sea (JES), Progress in Oceanography, 61, 193-211, 2004.

Yoon, J. M., Kim, J., Lee, J. H., Cho, H. K., Sohn, B.-J., and Ahn, M.-H. J. A.-P. J. o. A. S.: Retrieval of aerosol optical depth over East Asia from a geostationary satellite, MTSAT-1R, 43, 49-58, 2007.

https://doi.org/10.5194/amt-2020-336
Preprint. Discussion started: 17 September 2020

Atmospheric Measurement Techniques Discussions

Yoshida, M., Kikuchi, M., Nagao, T. M., Murakami, H., Nomaki, T., and Higurashi, A.: Common Retrieval of Aerosol Properties for Imaging Satellite Sensors, Journal of the Meteorological Society of Japan. Ser. II, 96B, 193-209, 2018.

Zhong, G., Wang, X., Tani, H., Guo, M., Chittenden, A., Yin, S., Sun, Z., and Matsumura, S.: A Modified Aerosol Free Vegetation Index Algorithm for Aerosol Optical Depth Retrieval Using GOSAT TANSO-CAI Data, Remote Sensing, 8, 2016.

https://doi.org/10.5194/amt-2020-336
Preprint. Discussion started: 17 September 2020


Atmospheric Measurement Techniques Discussions

Table 1. Satellite dataset used for the fusion products.

AOD type	F1	F2	F3	F4	FM1	FM2	FM3
AER	O	O	O	O	O	O	O
AMR	O		O	O	O		O
GV1				O	O		
GV2	O	O		O	O	O	

https://doi.org/10.5194/amt-2020-336
Preprint. Discussion started: 17 September 2020

Atmospheric Measurement Techniques Discussions

Table 2. RMSE values by time, AOD, and NDVI during KORUS-AQ, as used in this study.

AOD ≤ 0.5 / AOD >0.5	products	00 UTC	01 UTC	02 UTC	03 UTC	04 UTC	05 UTC	06 UTC	07 UTC
NDVI ≤ -0.1	AMR	0.109 / 0.232	0.109 / 0.141	0.1 / 0.134	0.104 / 0.157	0.1 / 0.165	0.111 / 0.189	0.098 / 0.206	0.125 / 0.211
	AES	0.074 / 0.185	0.073 / 0.196	0.072 / 0.187	0.067 / 0.365	0.066 / 0.421	0.063 / 0.396	0.059 / 0.324	0.05 / 0.261
	GV1	0.137 /0.145	0.114 / 0.158	0.124 / 0.204	0.109 / 0.198	0.119 / 0.169	0.125 / 0.183	0.123 / 0.194	0.124 / 0.204
	GV2	0.101 /0.182	0.107 / 0.154	0.113 / 0.257	0.113 / 0.235	0.125 / 0.242	0.108 / 0.276	0.121 / 0.243	0.115 / 0.204
-0.1 < NDVI ≤ 0.1	AMR	0.082 /0.142	0.093 / 0.202	0.132 / 0.17	0.154 / 0.226	0.102 / 0.217	0.101 / 0.172	0.112 / 0.195	0.149 / 0.224
	AES	0.067 /0.119	0.08 / 0.167	0.086 / 0.188	0.097 / 0.232	0.09 / 0.234	0.073 / 0.223	0.081 / 0.231	0.061 / 0.166
	GV1	0.107 /0.144	0.093 / 0.167	0.098 / 0.157	0.092 / 0.232	0.093 / 0.194	0.1 / 0.174	0.093 / 0.17	0.107 / 0.146
	GV2	0.098 / 0.164	0.105 / 0.205	0.107 / 0.216	0.111 / 0.294	0.098 / 0.229	0.106 / 0.231	0.092 / 0.2	0.089 / 0.184
-0.1 < NDVI ≤ 0.1	AMR	0.104 / 0.207	0.115 / 0.184	0.125 / 0.226	0.126 / 0.183	0.116 / 0.199	0.105 / 0.165	0.103 / 0.251	0.109 / 0.247
	AES	0.085 / 0.17	0.088 / 0.165	0.092 / 0.196	0.102 / 0.216	0.098 / 0.236	0.099 / 0.234	0.079 / 0.188	0.06 / 0.191
	GV1	0.094 / 0.188	0.1 / 0.222	0.118 / 0.211	0.111 / 0.2	0.087 / 0.193	0.102 / 0.228	0.118 / 0.19	0.115 / 0.26
	GV2	0.094 / 0.185	0.106 / 0.222	0.111 / 0.282	0.111 / 0.266	0.104 / 0.285	0.097 / 0.226	0.105 / 0.18	0.107 / 0.21
0.1 < NDVI ≤ 0.3	AMR	0.096 / 0.189	0.092 / 0.183	0.117 / 0.239	0.139 / 0.188	0.119 / 0.185	0.094 / 0.176	0.088 / 0.227	0.102 / 0.28
	AES	0.094 / 0.182	0.099 / 0.153	0.125 / 0.23	0.113 / 0.2	0.125 / 0.256	0.111 / 0.217	0.108 / 0.195	0.114 / 0.184
	GV1	0.071 / 0.17	0.072 / 0.165	0.092 / 0.249	0.102 / 0.156	0.114 / 0.264	0.104 / 0.157	0.078 / 0.206	0.053 / 0.23
	GV2	0.104 / 0.228	0.1 / 0.237	0.107 / 0.275	0.108 / 0.287	0.116 / 0.256	0.101 / 0.215	0.099 / 0.219	0.128 / 0.254
0.3 < NDVI ≤ 0.5	AMR	0.061 / NaN	NaN / NaN	NaN / NaN	NaN / NaN	NaN / NaN	NaN / NaN	NaN / NaN	NaN / NaN
	AES	0.076 / NaN	NaN / NaN	NaN / NaN	NaN / NaN	NaN / NaN	NaN / NaN	NaN / NaN	NaN / NaN
	GV1	0.076 / NaN	NaN / NaN	NaN / NaN	NaN / NaN	NaN / NaN	NaN / NaN	NaN / NaN	NaN / NaN
	GV2	0.067 / NaN	NaN / NaN	NaN / NaN	NaN / NaN	NaN / NaN	NaN / NaN	NaN / NaN	NaN / NaN

https://doi.org/10.5194/amt-2020-336
Preprint. Discussion started: 17 September 2020

Atmospheric Measurement Techniques Discussions

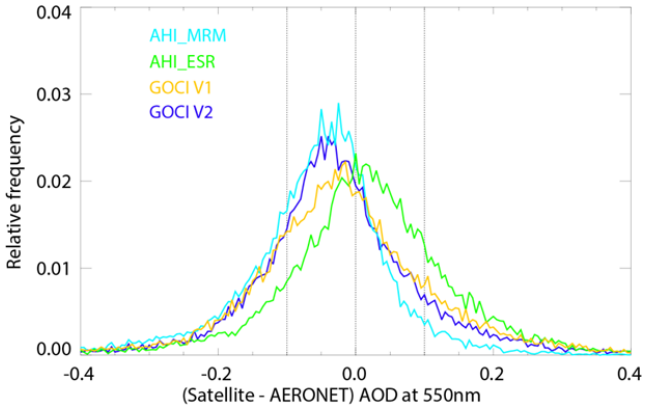

Figure 1. Comparison between observed AOD error distributions for AMR (cyan), AES (green), GV1 (yellow), and GV2 (blue).

https://doi.org/10.5194/amt-2020-336
Preprint. Discussion started: 17 September 2020

Atmospheric Measurement Techniques Discussions

Table 3. Systematic bias correction values for NDVI groups and temporal bins, for each satellite product from Gaussian fitting analysis used in MLE fusion.

	products	00 UTC	01 UTC	02 UTC	03 UTC	04 UTC	05 UTC	06 UTC	07 UTC
NDVI ≤ -0.1	AMR	-0.105	-0.060	-0.067	-0.125	-0.059	-0.026	-0.038	-0.067
	AES	-0.044	-0.001	0.006	0.022	0.009	0.020	0.001	-0.034
	GV1	-0.107	-0.069	-0.088	-0.072	-0.124	-0.109	-0.097	-0.106
	GV2	-0.046	0.002	0.079	-0.012	-0.025	-0.005	-0.141	-0.082
-0.1 < NDVI ≤ 0.1	AMR	-0.029	-0.003	-0.044	-0.017	-0.041	-0.016	-0.018	-0.046
	AES	0.009	0.005	0.022	0.046	0.068	0.035	0.037	-0.014
	GV1	-0.066	-0.038	-0.052	-0.056	-0.045	-0.042	-0.062	-0.085
	GV2	-0.033	0.116	-0.002	0.010	0.003	-0.024	-0.019	-0.051
-0.1 < NDVI ≤ 0.1	AMR	-0.028	-0.043	-0.141	-0.053	-0.028	-0.023	-0.048	-0.069
	AES	0.039	0.036	0.024	0.056	0.066	0.061	0.021	-0.020
	GV1	-0.055	-0.056	-0.036	-0.027	-0.021	-0.041	-0.068	-0.079
	GV2	-0.029	-0.046	0.037	0.036	0.055	0.025	-0.037	-0.060
0.1 < NDVI ≤ 0.3	AMR	-0.077	-0.052	-0.072	-0.062	-0.047	-0.059	-0.062	-0.076
	AES	0.033	0.044	-0.011	0.046	0.074	0.051	0.084	-0.020
	GV1	-0.111	-0.039	-0.051	-0.049	-0.065	-0.027	-0.044	-0.177
	GV2	-0.05	-0.004	-0.090	0.061	-0.041	-0.105	-0.044	-0.215
0.3 < NDVI ≤ 0.5	AMR	-0.03	NaN	NaN	NaN	NaN	NaN	NaN	NaN
	AES	0.065	NaN	NaN	NaN	NaN	NaN	NaN	NaN
	GV1	-0.11	NaN	NaN	NaN	NaN	NaN	NaN	NaN
	GV2	-0.27	NaN	NaN	NaN	NaN	NaN	NaN	NaN

https://doi.org/10.5194/amt-2020-336
Preprint. Discussion started: 17 September 2020

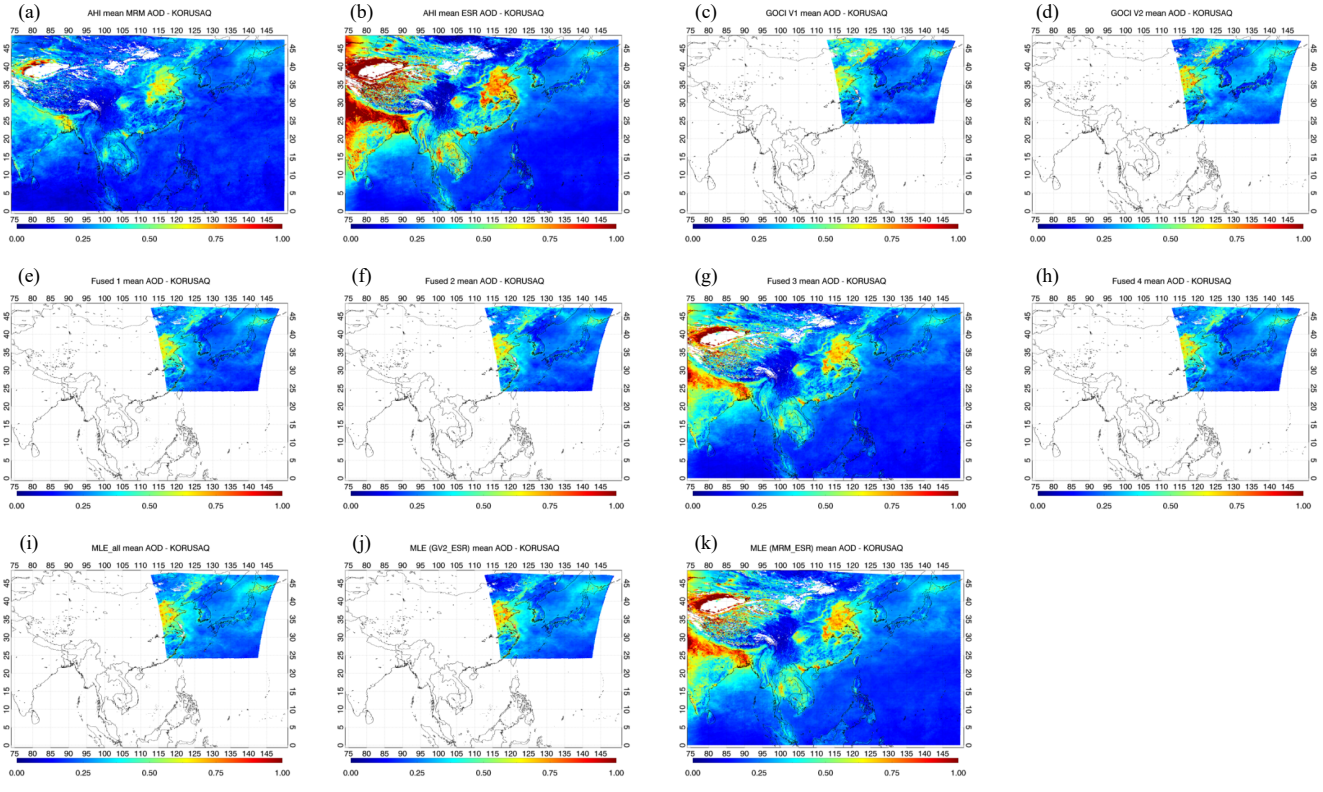

Figure 2. Images of average AOD from each satellite product and fusion product; (a) AMR, (b) AES, (c) GV1, (d) GV2, (e) F1, (f) F2, (g) F3, (h) F4, (i) FM1, (j) FM2, and (k) FM3 during KORUS-AQ campaign.

https://doi.org/10.5194/amt-2020-336
Preprint. Discussion started: 17 September 2020

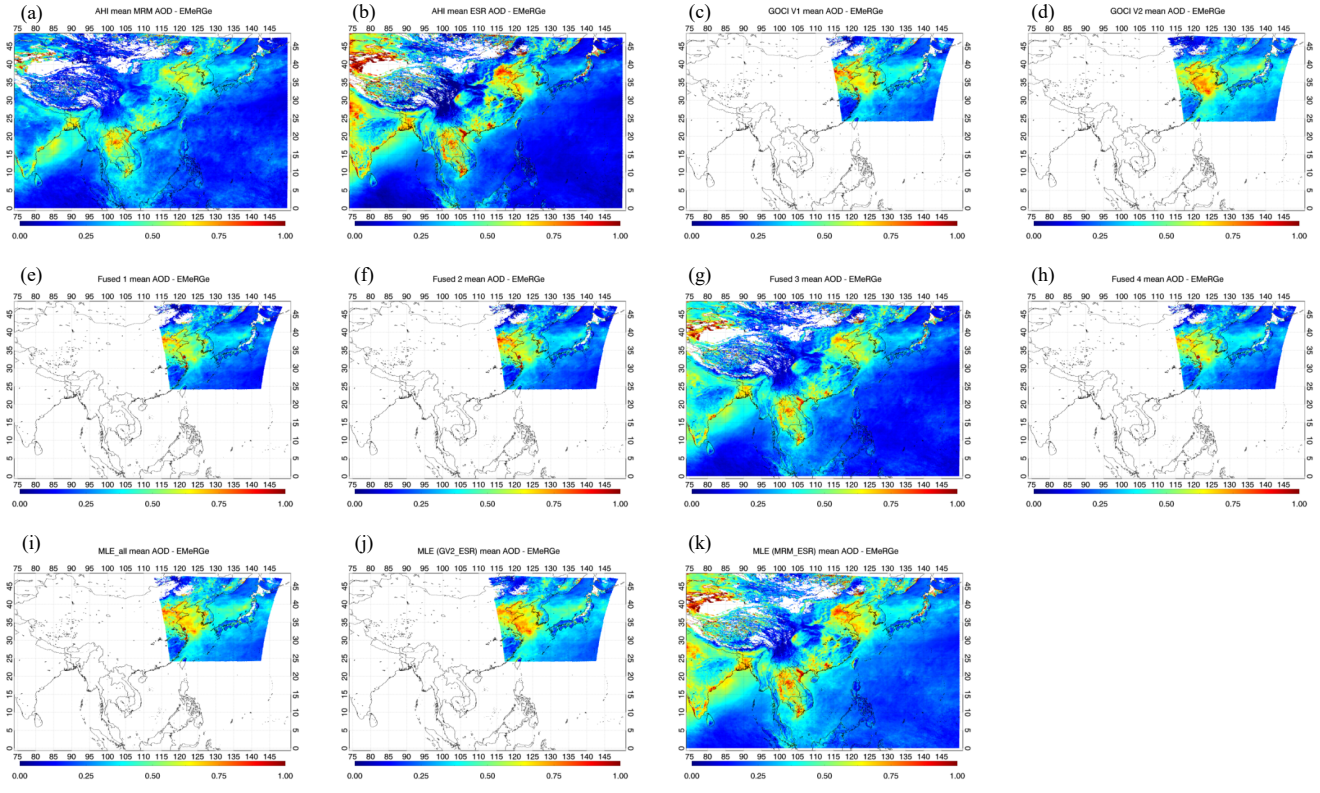

Figure 3. Same as Figure 2, but for EMeRGe campaign.

https://doi.org/10.5194/amt-2020-336
Preprint. Discussion started: 17 September 2020

Atmospheric Measurement Techniques Discussions

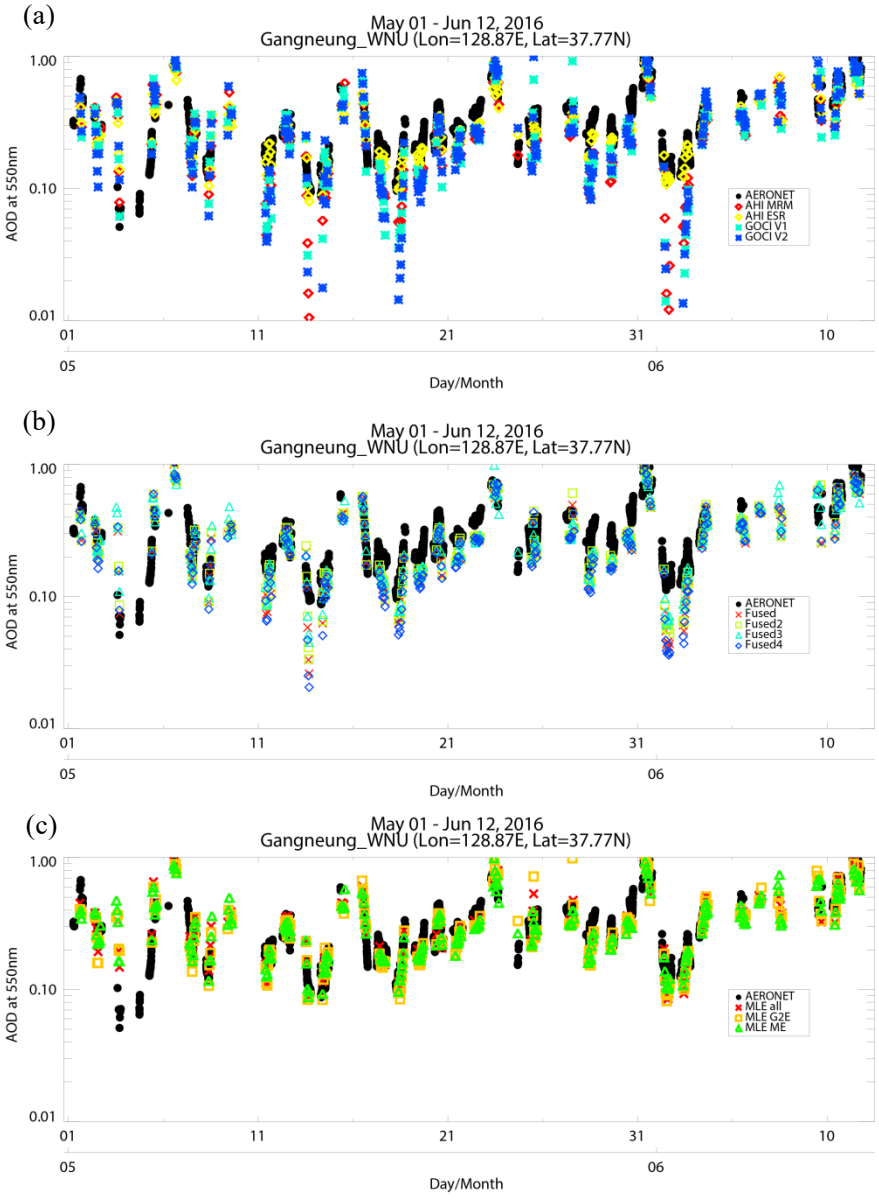

Figure 4. Time series of the (a) respective satellite-derived, (b) ensemble mean, and (c) MLE fusion AODs at Gangneung_WNU site during KORUS- AQ period..

https://doi.org/10.5194/amt-2020-336
Preprint. Discussion started: 17 September 2020

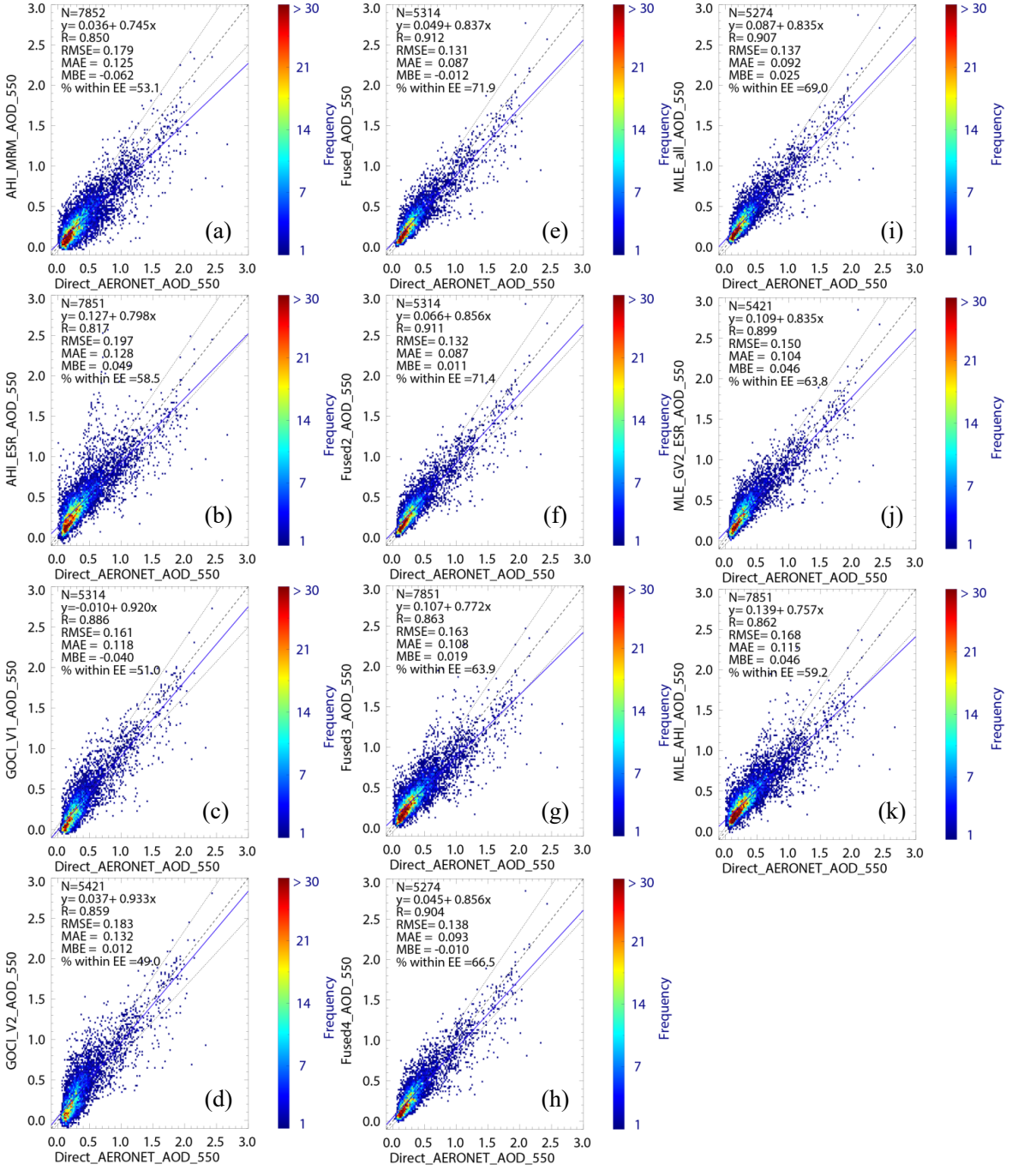

Figure 5. Comparison of four respective satellite products (a) AMR, (b) AES, (c) GV1, (d) GV2, four ensemble mean products (e) F1, (f) F2, (g) F3, (h) F4, and three MLE products (i) FM1, (j) FM2, (k)FM3 AOD with AERONET/SONET.AOD

https://doi.org/10.5194/amt-2020-336
Preprint. Discussion started: 17 September 2020

Atmospheric Measurement Techniques Discussions

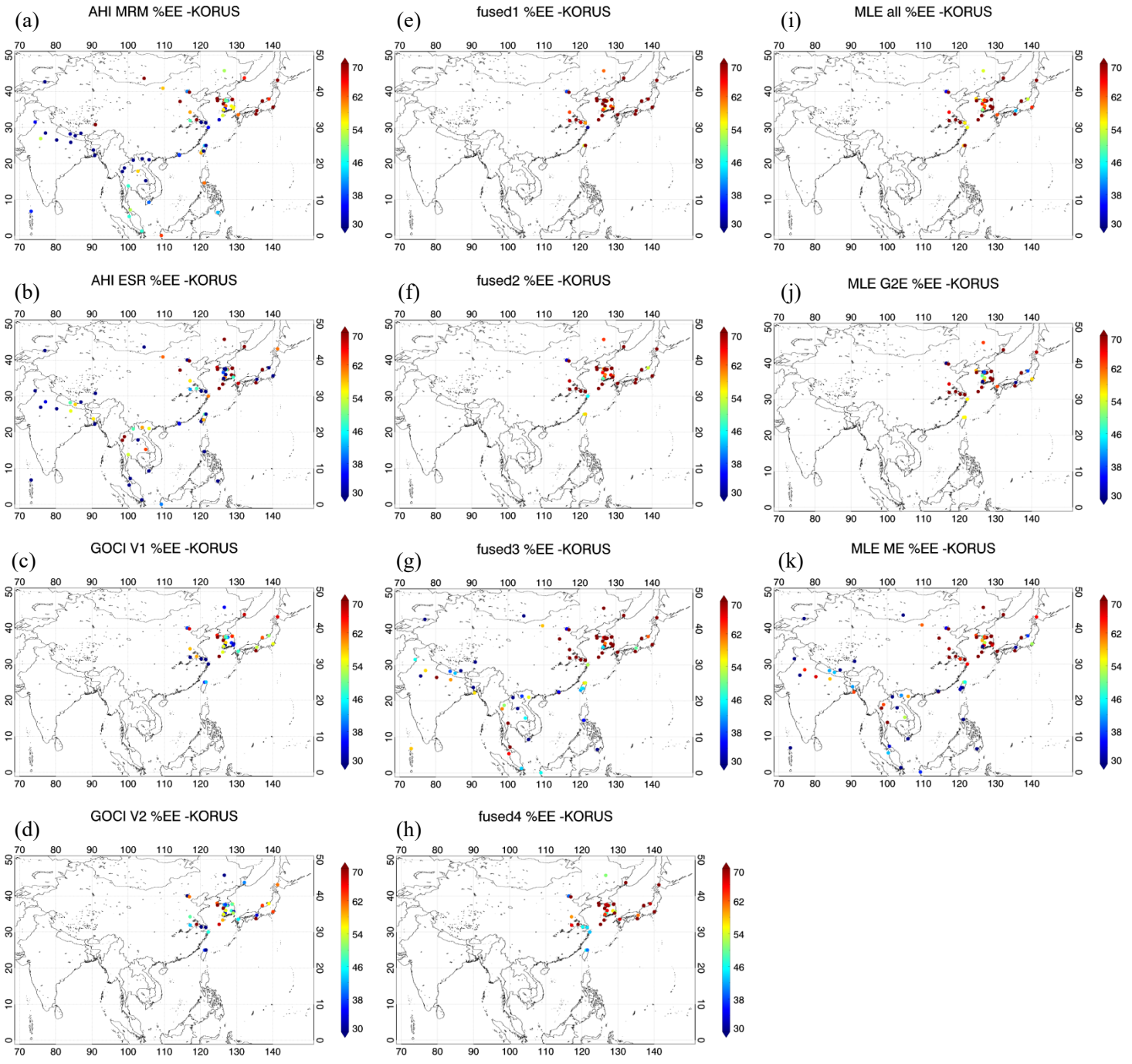

Figure 6. Spatial distribution of %EE for (a) AMR, (b) AES, (c) GV1, (d) GV2, (e) F1, (f) F2, (g) F3, (h) F4, (i) FM1, (j) FM2, and (k) FM3AOD during KORUS-AQ campaign.

https://doi.org/10.5194/amt-2020-336
Preprint. Discussion started: 17 September 2020

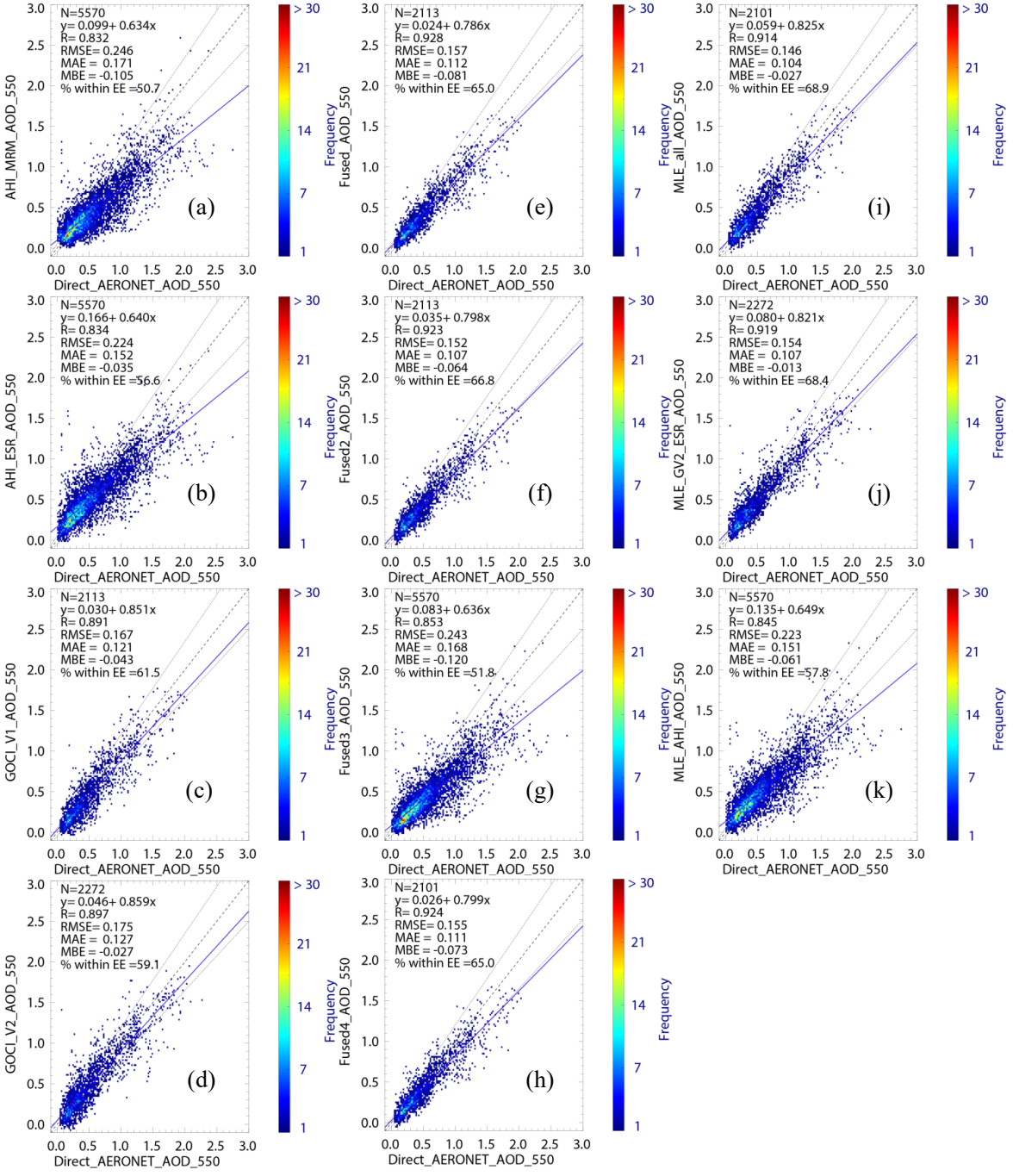

Figure 7. Same as Figure 5, but for EMeRGe campaign

https://doi.org/10.5194/amt-2020-336
Preprint. Discussion started: 17 September 2020

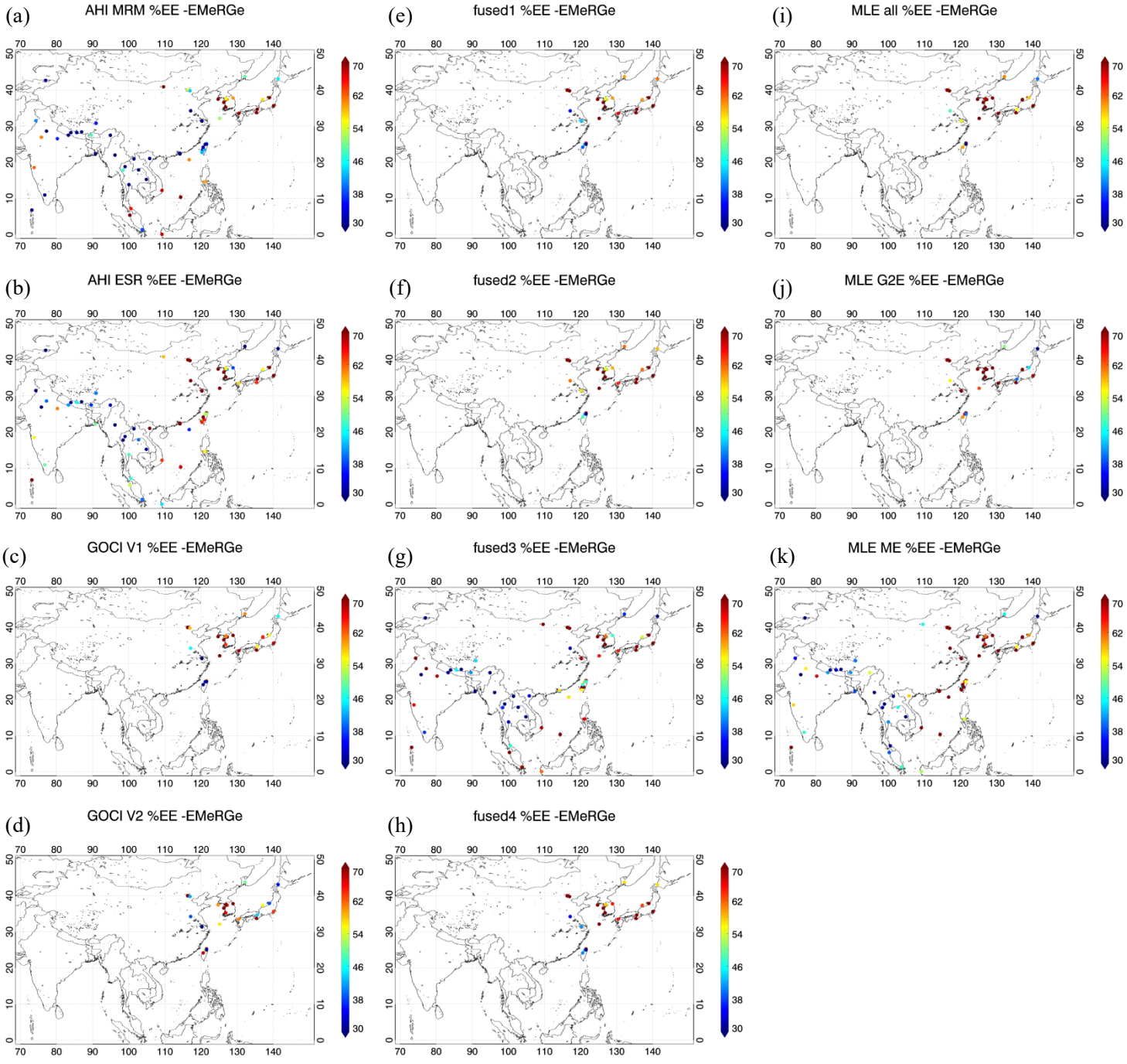

Figure 8. Same as Figure 5, but for EMeRGe campaign

https://doi.org/10.5194/amt-2020-336
Preprint. Discussion started: 17 September 2020

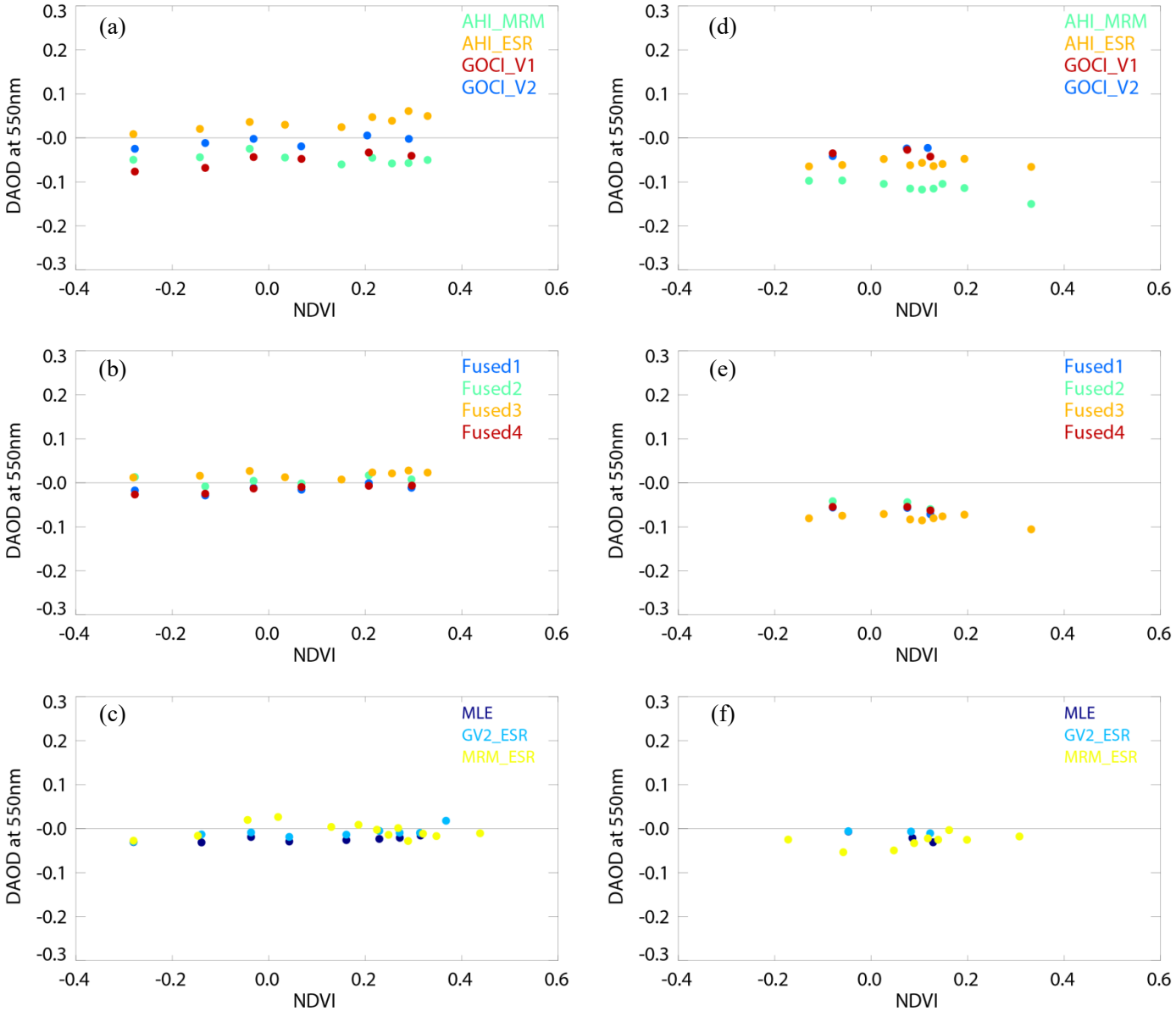

Figure 9. Difference between (a, d) respective, (b, e) ensemble-mean, or (c,f) MLE and AERONET/SONET AOD in terms of NDVI during the KORUS-AQ (left column) and EMeRGe (right column) campaigns

https://doi.org/10.5194/amt-2020-336
Preprint. Discussion started: 17 September 2020

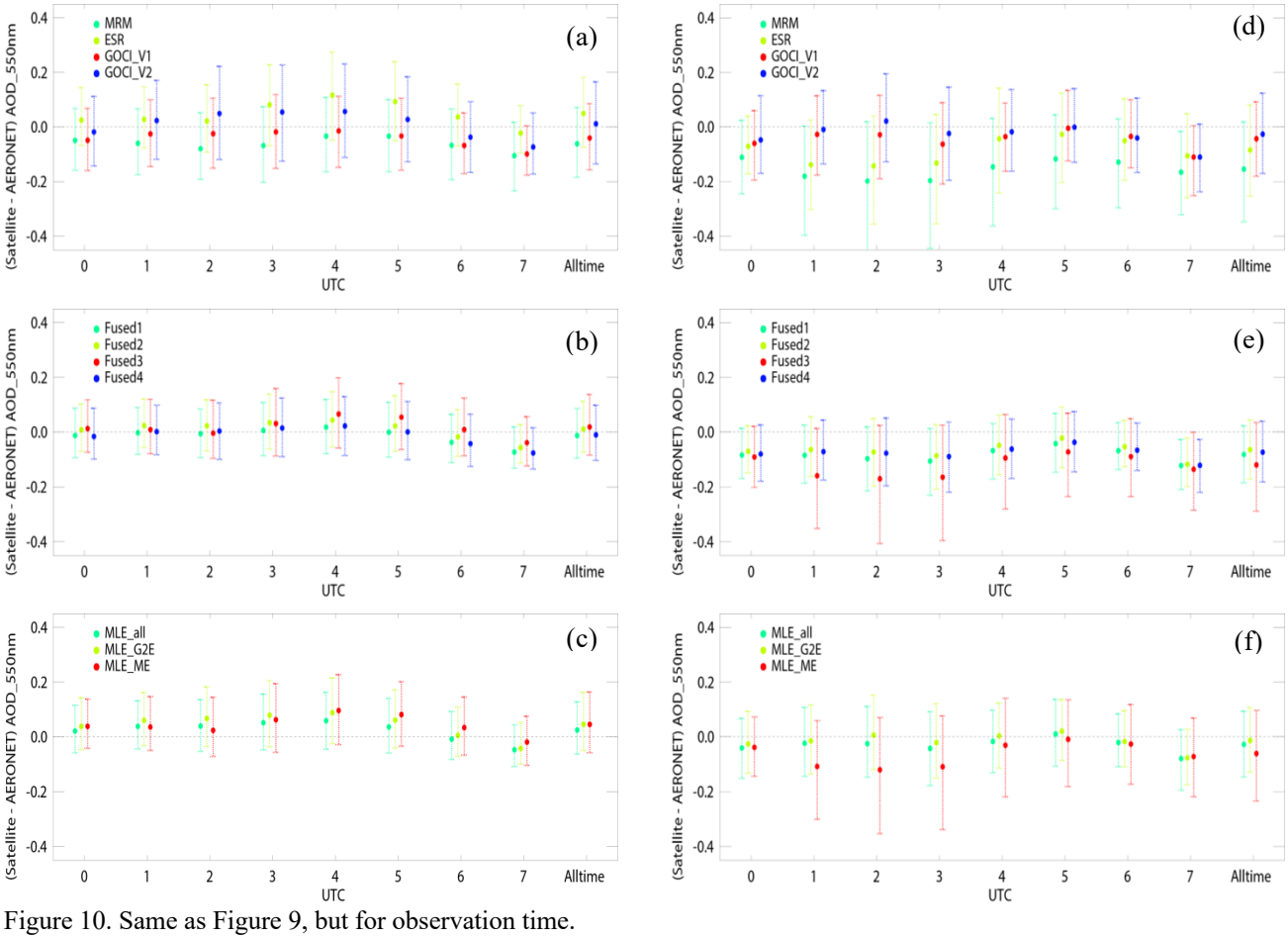

Figure 10. Same as Figure 9, but for observation time.

https://doi.org/10.5194/amt-2020-336
Preprint. Discussion started: 17 September 2020

Atmospheric Measurement Techniques Discussions

10

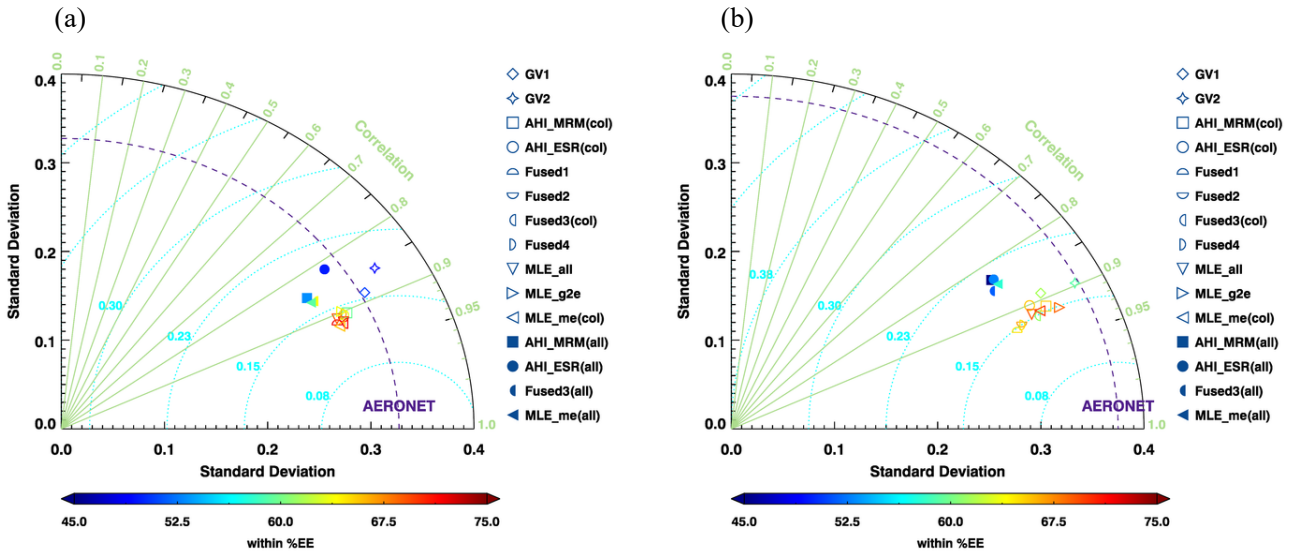

Figure 11. Taylor diagrams comparing the respective, ensemble-mean, and MLE AODs and values obtained from AERONET during the (a) KORUS-AQ and (b) EMeRGe periods.